PCCP

ROYAL SOCIETY OF CHEMISTRY

TUTORIAL REVIEW

View Article Online
View Journal | View Issue

Cite this: *Phys. Chem. Chem. Phys.*, 2024, **26**, 15068

Transmission line revisited – the impedance of mixed ionic and electronic conductors†

Andreas E. Bumberger, Andreas Nenning and Juergen Fleig *

This contribution provides a comprehensive guide for evaluating the one-dimensional impedance response of dense mixed ionic and electronic conductors based on a physically derived transmission line model. While mass and charge transport through the bulk of a mixed conductor is always described by three fundamental parameters (chemical capacitance, ionic conductivity and electronic conductivity), it is the nature of the contact interfaces that largely determines the observed impedance response. Thus, to allow an intuitive adaptation of the transmission line model for any specific measurement situation, the physical meanings of terminal impedance elements at the ionic and electronic rail ends are explicitly discussed. By distinguishing between charge transfer terminals and electrochemical reaction terminals, the range of possible measurement configurations is categorized into symmetrical, SOFC-type and battery-type setups, all of which are explored on the basis of practical examples from the literature. Also, the transformation of an SOFC electrode into a battery electrode and the relevance of side reactions for the impedance of battery electrodes is discussed.

Received 5th March 2024,
Accepted 8th May 2024

DOI: 10.1039/d4cp00975d

rsc.li/pccp

Introduction

Electrochemical impedance spectroscopy (EIS) has become an indispensable tool for studying the thermodynamic and kinetic properties of mixed ionic and electronic conductors (MIECs). In the field of solid-state ionics, the most prominent classes of MIECs include intercalation electrodes for batteries (*e.g.* $Li_{1-\delta}CoO_2$ (LCO)), high-temperature mixed-conducting electrodes for solid oxide cells (*e.g.* $La_{0.6}Sr_{0.4}CoO_{3-\delta}$ (LSC)), and imperfect electrolytes (*e.g.* gadolinium-doped ceria (GDC) or $Li_{0.29+\delta}La_{0.57}TiO_3$ (LLTO) under reducing conditions). By applying a low-amplitude voltage or current perturbation onto an electrochemical system, impedance spectroscopy allows the separation of transport processes in the frequency domain according to their characteristic time constants. Generally, the more chemically and morphologically complex a system, the larger the variety of transport processes and time constants that potentially contribute to the overall impedance spectrum. As a result, intricate equivalent circuits with a large number of parameters are required to adequately describe the impedance response of, for example, a porous lithium-ion battery (LIB) or solid oxide fuel or electrolyser cell (SOFC/SOEC) electrode.[1–4]

Institute of Chemical Technologies and Analytics, TU Wien, Vienna, Austria.
E-mail: juergen.fleig@tuwien.ac.at

† Electronic supplementary information (ESI) available. See DOI: https://doi.org/10.1039/d4cp00975d

However, even if morphological complexities such as porosity or tortuosity can be excluded and a well-defined, single-crystalline MIEC sample is measured, the analysis of the recorded impedance spectra is often far from trivial, mainly for two reasons. First, although the bulk electrochemical properties of a mixed conductor are described by only three independent parameters (see below), these can vary over orders of magnitude, depending on the chemical potential of the relevant neutral species. For example, the electrochemical properties of LIB electrode materials are strongly dependent on the state-of-charge (SOC), *i.e.* the Li content.[5–7] Analogously, the transport properties of SOFC and SOEC materials vary with the oxygen content.[8] The second reason for the large variety of MIEC impedance spectra is found in the boundary conditions for ionic and electronic transport at the contact interfaces, which necessarily contribute to the measured impedance spectra. In the simplest case, the contacts are either fully blocking or reversible (non-blocking) for ions and/or electrons. Unfortunately, this qualitative black-and-white distinction is rarely realized in experiments, meaning that the magnitudes of the corresponding interfacial resistances and capacitances for both ionic and electronic charge carriers must be taken into account.

The extraction of physically meaningful solid-state electrochemical properties from an MIEC impedance spectrum requires an equivalent circuit that is based on the underlying differential equations describing the transport of mass and charge in the presence of electrical and chemical potential gradients. The one-dimensional particle flux density J_i of a

charged species i is described by the Nernst–Planck equation,[9,10] which reads

$$J_i(x,t) = -D_i\frac{\partial c_i(x,t)}{\partial x} - \frac{\sigma_i(x,t)}{z_i e}\frac{\partial \Phi(x,t)}{\partial x}, \quad (1)$$

with the diffusion coefficient D_i, concentration c_i, position x along the direction of transport, time t, conductivity σ_i, charge number z_i, elementary charge e, and electrical potential Φ. More descriptively, eqn (1) is often referred to as the diffusion-drift equation, as it separately considers the mass and charge transport contributions from diffusion (Fick's law, concentration gradient) and drift (Ohm's law, electrical potential gradient). In principle, eqn (1) can be solved for a specific experimental situation and several charge carriers by inserting the appropriate boundary conditions defined by the sample and setup. An impedance expression can then be obtained by relating J_i to the electrical current density. However, this approach suffers from two major limitations. First, analytical solutions to eqn (1) often rely on simplifying assumptions, such as neglecting the drift term for $\sigma_{eon} \gg \sigma_{ion}$ (subscripts eon and ion indicating electronic and ionic species, respectively).[11] For more complicated systems, numerical solutions are required,[12] making the impedance analysis of MIEC devices a tedious task. Moreover, even when an analytical expression can be obtained, it is unclear how to appropriately use it in a full equivalent circuit that considers contacts and other contributions to the measured impedance. Equivalent circuits are therefore often constructed intuitively in order to reproduce the given shape of a spectrum. However, the interpretation of such circuits may easily contradict the fundamental laws of electron and ion transport in mixed conductors.

As first proposed by Jamnik and Maier,[13–15] and later in a more comprehensive form by Lai and Haile,[9] these problems can be circumvented by mapping eqn (1) itself onto an equivalent circuit before applying any simplifying assumptions or boundary conditions. For a one-dimensional current flow across an MIEC slab of area A and thickness L, this results in a general transmission line circuit, featuring two parallel resistive rails for ion and electron conduction with small resistive increments r_{ion} and r_{eon}, which are coupled by incremental chemical capacitors c_{chem}, as shown in Fig. 1a. The total ionic and electronic resistances are thus given by $R_{ion} = \sum r_{ion}$, $R_{eon} = \sum r_{eon}$, and the total chemical capacitance is $C_{chem} = \sum c_{chem}$. At the rail ends, terminal impedance elements Z_i account for the interfacial processes of ions and electrons taking place at the contact/MIEC boundaries. In many cases, $R|C$ elements may be used to describe the terminal impedances Z_i, *cf.* Fig. 1b and c. The dielectric bulk capacitance C_{diel} of the MIEC is connected in parallel to the entire transmission line.

The equivalence of this transmission line and the underlying transport equations becomes more visible when expressing the electronic and ionic current densities (j_{eon}, j_{ion}) by the gradients of electrochemical potentials of the respective species ($\nabla\tilde{\mu}_{eon}$, $\nabla\tilde{\mu}_{ion}$) with $\tilde{\mu}_i = \mu_i + z_i e\Phi$, μ_i being the chemical potential of species i. In the one-dimensional case we then have

$$j_{eon} = -\sigma_{eon}\frac{\partial}{\partial x}\frac{\tilde{\mu}_{eon}}{z_{eon}e} \quad (2)$$

for electrons and

$$j_{ion} = -\sigma_{ion}\frac{\partial}{\partial x}\frac{\tilde{\mu}_{ion}}{z_{ion}e} \quad (3)$$

for ions. Due to charge neutrality in the bulk, the total electrical current ($j_{eon} + j_{ion}$) cannot vary spatially. However, coupling between electronic and ionic current at the same location is possible and causes a change of the mobile species concentration or, more generally, of the concentration c_a of the formally neutral (atomic) species a, defined by a = ion + z_{ion}·eon (*e.g.* O = O^{2-}–$2e^-$). We thus find

$$\frac{\partial}{\partial x}j_{ion} = -\frac{\partial}{\partial x}j_{eon} = -z_{ion}e\frac{\partial}{\partial t}c_a. \quad (4)$$

In contrast to conduction processes, charge transfer between the ion and electron rails only takes place until a new steady state concentration c_a is reached. Mathematically, the corresponding concentration change is described by the so-called chemical capacitance (C_{chem}), see below.

An analytical impedance expression of the transmission line circuit was originally only derived for symmetrical contacts,[9] *i.e.* for $Z_A = Z_C$, $Z_B = Z_D$. However, the impedance of the circuit can also be expressed analytically for the general case of four different Z_i by adapting the derivation in ref. 9 for four distinct terminals.[16] This is essential for inherently non-symmetrical MIEC devices such as battery electrodes. The full impedance expression of the transmission line in Fig. 1a can be found in ref. 16 and is also provided in a slightly modified nomenclature as ESI† to this paper in the form of a *Matlab* script. The reader is encouraged to use this script for simulations and explore how the impedance spectrum changes in response to a variation of interface and material parameters. Furthermore, the equivalent circuit has been implemented in the impedance analysing software *ZView* upon request (distributed element DX type 34).

In contrast to the underlying differential equations, the general transmission line can easily be adapted and simplified for specific experimental situations and also allows a physically meaningful integration of the solid-state transport impedance into larger equivalent circuits. Moreover, it provides a highly intuitive approach to understanding the impedance of MIECs and a common root for the impedance responses of different types of MIEC devices. However, this relies on a correct and physically meaningful interpretation and use of the terminal impedances, which is not always straightforward and requires further considerations.

In this contribution, we provide a practical guide for applying the transmission line model to a wide range of measuring geometries and devices commonly encountered in solid-state electrochemical research, including batteries, solid oxide cells and symmetrical two-electrode setups for the characterisation of MIECs and solid electrolytes. The physical meanings of the terminal impedances are discussed and rules are introduced in

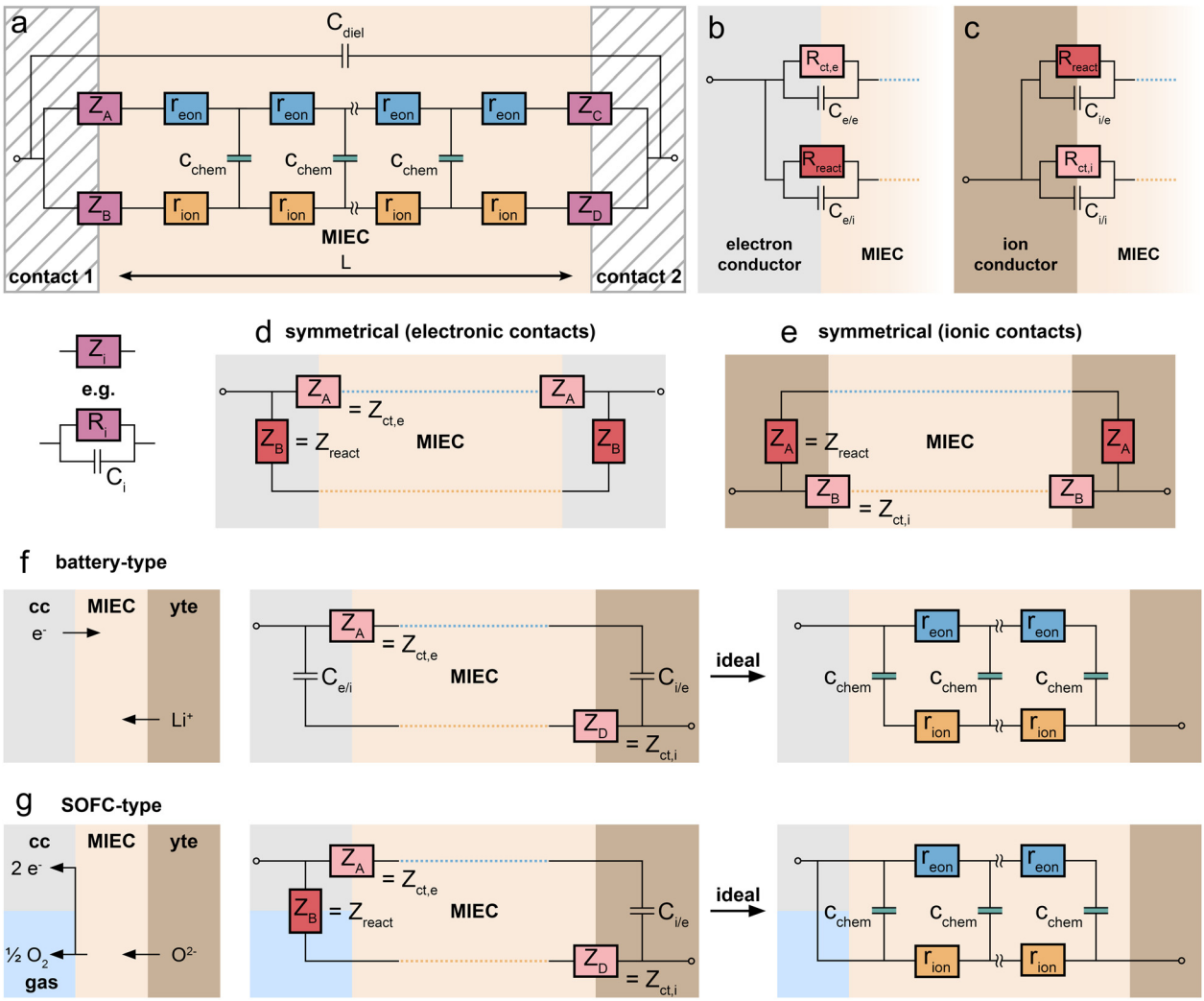

Fig. 1 (a) General one-dimensional transmission line model for the transport of mass and charge across a MIEC slab of area A and thickness L. The circuit consists of two parallel resistive rails for electronic and ionic transport, coupled by chemical capacitors. Two different contacts define the terminal impedances for electrons (Z_A, Z_C) and ions (Z_B, Z_D). The bulk dielectric capacitance of the MIEC is connected in parallel to the transmission line. (b) Terminal impedance elements at the interface between electron conductor and MIEC. (c) Terminal impedance elements at the interface between ion conductor and MIEC. (d) Schematic representation of a symmetrical measurement setup with electronic contacts. (e) Schematic representation of a symmetrical measurement setup with ionic contacts. (f) Sketch and interfacial impedance elements of a battery-type setup, with the MIEC sandwiched between current collector (cc) and electrolyte (yte). (g) Sketch and interfacial impedance elements of an SOFC-type setup, with the MIEC sandwiched between current collector/oxygen atmosphere and electrolyte. The idealised circuits on the r.h.s. of (f) and (g) neglect interfacial capacitances and resistances.

order to help deciding which of the terminating R and C elements are essential or negligible in certain cases. We provide specific application examples from current research and also discuss the limitations of approaches that rely on traditional Warburg elements by relating them back to the transmission line model. Furthermore, we emphasize the close relationship between different types of MIEC devices and show how minor experimental adjustments may transform the transmission line from one device type to another. Thus, our work is aimed at improving the intuitive understanding of MIEC impedance spectra and providing a practical approach for the derivation of tailored equivalent circuits for any specific experimental situation.

Interfacial impedances and specification of case studies

In principle, MIECs might be contacted by other MIECs, by ionic conductors (electrolytes) or by electron conductors (*e.g.* metals). Here, we restrict ourselves to the (very common) cases of MIECs being contacted either by a pure electron conductor or a pure ion conductor. Then, one charge carrier can move directly between contact and MIEC, whereas the other carrier can only enter or leave the MIEC if an electrochemical coupling reaction at the interface takes place. As a consequence, also the electrochemical processes causing the interfacial impedances of the two rails become different. In other words: Z_A and Z_B

(or Z_C and Z_D) are fundamentally different. This is specified in the following.

For the charge carrier that can also move in the contact material (electrons in a metal contact, ions in an electrolytic contact), the resistive part of the corresponding interfacial impedance is "simply" a charge transfer resistance between two phases. We thus denote this terminal impedance as "charge transfer impedance" Z_{ct}. Space charge regions but also chemical energy barriers between the two phases may play a crucial role here. For electrons, for example, the situation can be very similar to a Schottky contact on a semiconductor. In many cases this charge transfer impedance may be described by a charge transfer resistance R_{ct} in parallel to an interfacial capacitance. The latter is charged by changing the interfacial charge carrier concentrations in both phases, for example by changing the corresponding space charge(s). These changes, however, only refer to the charge carrier which is mobile in both phases (*e.g.* electrons for an electronic contact) and are denoted as $C_{e/e}$ and $C_{i/i}$ for the electronic or ionic rail, respectively.

The charge carrier in the MIEC which cannot move in the contact material (*e.g.* ions in the electronic contact) has fundamentally different boundary conditions. The only way to still get a DC current of this charge carrier in the MIEC *via* the respective rail is by means of an electrochemical reaction, which couples the ions in the MIEC to the electrons in the contact or *vice versa*. For graphical differentiation, this element (Z_{react}) is drawn vertically. For oxygen ion conducting MIECs, a typical electrochemical coupling reaction is the oxygen exchange reaction $1/2O_2 + 2e^- \rightleftharpoons O^{2-}$, for example at a porous metal electrode. For a metal ion conducting MIEC, on the other hand, reduction of a metal ion and its deposition on the electrode may take place. The reaction $Li^+ + e^- \rightleftharpoons Li^0$, for example, enables a Li^+ current without any contact of the MIEC to a lithium-ion conductor.

This second type of interfacial terminal impedance may exist on both rails, for the ionic rail at the electronic contact and for the electronic rail at the ionic contact. We label it reaction or coupling impedance Z_{react}, and its resistive part is represented by the resistance R_{react}, which reflects the kinetics of the corresponding electrochemical reaction. In parallel to this resistor, again a parallel capacitor $C_{i/e}$ (or $C_{e/i}$) comes into play. This capacitor, however, resembles more the electrolytic double layer capacitance known from electrochemistry, with ions accumulating at one side of the interface and electrons on the other. In Fig. 1b and c, the two different types of interfaces are sketched, both with two different terminal elements. Interfaces without any electrochemical reaction lead to infinitely large coupling resistances R_{react}. The corresponding charge carrier is then fully blocked and the terminating impedance is reduced to a capacitor. Interfaces with finite coupling resistances are (at least partly) transmissive for the corresponding charge carrier. However, it should be noted that the treatment of the four terminal impedances as $R|C$ elements is an approximation of the exact, usually not analytically solvable set of boundary conditions.[14]

Having clarified the different types of terminating elements, we may now specify typical measurement situations. When analysing the material properties of an MIEC, we often rely on a (geometrically) symmetrical situation, *i.e.* the use of the same type of contact on both sides of the MIEC. This situation is sketched in Fig. 1d and e, where the reaction impedances Z_{react} are drawn in a vertical position to emphasise their role as coupling elements between the two resistive rails. Numerous examples of such symmetrical situations are discussed in this paper, first for a pure electrolyte and then for MIECs with either electrons or ions being blocked.

A very different situation is found for MIEC electrode materials used in lithium-ion batteries. It is far beyond the scope of this paper to consider the impedance of typical porous electrodes; for this the reader is referred to ref. 2 and 3. Here, we restrict our discussion to the very basic features of a dense MIEC used as a battery electrode in a one-dimensional manner. Contacting of such battery-type electrodes is asymmetrical per definition, as shown in Fig. 1f: on one side of the MIEC an electrolyte supplies ions and on the other side the current collector transfers electrons. Electrochemical (coupling) reactions at both contacts should be absent and the corresponding Z_{react} are thus essentially capacitive. Accordingly, the corresponding transmission line is antisymmetrical, at least in terms of circuit elements, even though the absolute values of the corresponding elements are generally different. If charge transfer resistances are negligible as well, the battery-type situation simplifies to the antisymmetrical circuit in Fig. 1f (r.h.s.), provided $C_{chem} \gg C_{e/i}$ and $C_{i/e}$, respectively.

This changes when moving to situations typical for MIEC electrode materials used in SOFCs/SOECs, such as (La,Sr)$FeO_{3-\delta}$ (LSF), (La,Sr)$CoO_{3-\delta}$ (LSC), (La,Sr)(Co,Fe)$O_{3-\delta}$ (LSCF) or (La,Sr)$MnO_{3-\delta}$ (LSM), *etc.* Again, we do not consider the case of porous electrodes with their complex interplay of mixed conduction, gas diffusion and electrochemical reaction. Rather, we restrict ourselves to quasi-one-dimensional electrodes (*e.g.* thin film electrodes), *cf.* sketch in Fig. 1g. On the electrolyte side of the MIEC, electrons should be completely blocked, *i.e.* electrochemical reactions should not occur at all. At the opposite (electronic current collector) side, however, ions should not be blocked in fuel cell application. Rather, electrochemical reactions have to take place, with R_{react} being as low as possible.

More specifically, electrochemical reactions such as oxygen evolution or oxygen reduction according to $1/2O_2 + 2e^- \rightleftharpoons O^{2-}$ have to occur at such electrode/contact interfaces. Accordingly, a truly asymmetrical situation results. Actually, this takes us to the limits of the one-dimensional model since the corresponding reactions do not take place at the current collector/MIEC interface but mostly at the free MIEC surface or at the three-phase boundary. In any case this violates the one-dimensionality of the current flow. However, with a proper positioning of current collectors we may still treat such MIECs in a one-dimensional manner when representing the electrochemical reaction at the corresponding MIEC/contact interface by the terminal impedance $Z_B = Z_{react} = R_{react}|C_{e/i}$.

These three prototypical situations are all further discussed and exemplified in the course of this paper. In particular, it is shown how the terminal elements can be treated, and often simplified, for specific situations and examples. First, however, we want to further specify the basic elements of the transmission line model, relate them to the chemical diffusion coefficient and discuss this also in the context of another transmission line model very common in the field – the Warburg impedance.

Solid-state diffusion and Warburg elements

Basic circuit elements and ambipolar transport

According to the transmission line model, three parameters describe the bulk properties of an MIEC – the chemical capacitance C_{chem}, the ionic conductivity σ_{ion}, and the electronic conductivity σ_{eon}. The electronic and ionic conductivities can each be quantified by a mobility u_i and a concentration of mobile charge carriers c_i of charge number z_i according to

$$\sigma_i = |z_i| e c_i u_i. \tag{5}$$

It is often convenient to consider concentrations and mobilities on a defect level, *e.g.* vacancies for ions.

The volume-specific chemical capacitance is defined as[13,14]

$$C_{\mathrm{chem}}^{\mathrm{V}} = \frac{C_{\mathrm{chem}}}{V} = {z_{\mathrm{ion}}}^2 e^2 \left(\frac{\partial \mu_{\mathrm{a}}}{\partial c_{\mathrm{a}}}\right)^{-1}, \tag{6}$$

where μ_{a} is the chemical potential of the relevant atomic species a, and V denotes the sample volume. For example, in a mixed conducting oxide, where $z_{\mathrm{ion}} = -2$, the chemical capacitance is related to the oxygen chemical potential *via*

$$C_{\mathrm{chem}}^{\mathrm{V}} = 4e^2 \left(\frac{\partial \mu_{\mathrm{O}}}{\partial c_{\mathrm{O}}}\right)^{-1}. \tag{7}$$

Phenomenologically speaking, the chemical capacitance reflects the material's capacity to store charge by varying its stoichiometry. For example, when oxygen ions are incorporated from the electrolyte into an SOEC anode material, they can either move through the electrode and leave it at the surface as molecular oxygen (with electrons entering the current collector) or stay in the anode and thereby increase the oxygen content of the material.[8,17] Due to charge neutrality, also in the second case electrons have to be transferred to the current collector, and thus an electrical current flows through the external circuit.

For LIB electrode materials, the stoichiometry change described by the chemical capacitance

$$C_{\mathrm{chem}}^{\mathrm{V}} = e^2 \left(\frac{\partial \mu_{\mathrm{Li}}}{\partial c_{\mathrm{Li}}}\right)^{-1} \tag{8}$$

is equivalent to the differential capacity (or $\mathrm{d}Q/\mathrm{d}V$).[5,7] It describes the thermodynamics of Li insertion, consisting of Li^+ insertion from the electrolyte and the compensating electron transfer from the current collector.

Obviously, on a phenomenological level, neutral atoms (either oxygen or lithium in the examples above) have to move in an MIEC to finally change its composition. This is realized by an electroneutral combined motion of ions and electrons, called ambipolar or chemical transport. This ambipolar transport can be quantified by two ambipolar properties – the ambipolar conductivity $\tilde{\sigma}$ and the ambipolar (or chemical) diffusion coefficient $\tilde{D}$. The ambipolar conductivity

$$\tilde{\sigma} = \frac{\sigma_{\mathrm{eon}}\sigma_{\mathrm{ion}}}{\sigma_{\mathrm{eon}} + \sigma_{\mathrm{ion}}} \tag{9}$$

relates the particle flux density of the atoms a (and thus also of the corresponding ions) to the chemical potential of atoms μ_{a} (*e.g.* μ_{O} or μ_{Li}) *via*

$$J_{\mathrm{a}} = -\frac{\tilde{\sigma}}{{z_{\mathrm{ion}}}^2 e^2} \nabla \mu_{\mathrm{a}}. \tag{10}$$

This property is decisive, for example, for quantifying a steady-state flux across an MIEC.

The chemical diffusion coefficient describes the time dependence of stoichiometry changes according to Fick's law of diffusion

$$J_{\mathrm{a}} = -\tilde{D} \nabla c_{\mathrm{a}}. \tag{11}$$

The chemical diffusion coefficient and the ambipolar conductivity are related *via* the chemical capacitance[18] according to

$$\tilde{D} = \frac{\tilde{\sigma}}{C_{\mathrm{chem}}^{\mathrm{V}}}. \tag{12}$$

Hence, material changes that increase both $\tilde{\sigma}$ and $C_{\mathrm{chem}}^{\mathrm{V}}$ may finally leave $\tilde{D}$ unperturbed.

Assuming a one-dimensional geometry, *i.e.* transport across an MIEC slab of area A and thickness L, we thus find

$$\tilde{D} = \frac{L^2}{(R_{\mathrm{ion}} + R_{\mathrm{eon}}) C_{\mathrm{chem}}} = \frac{L^2}{\tau}, \tag{13}$$

with the time constant of stoichiometry change

$$\tau = (R_{\mathrm{ion}} + R_{\mathrm{eon}}) C_{\mathrm{chem}} \tag{14}$$

or

$$\tau = \frac{C_{\mathrm{chem}}^{\mathrm{V}} L^2}{\tilde{\sigma}}. \tag{15}$$

Please note that for symmetrical samples (Fig. 2b), only half the sample thickness ($L/2$) enters into the time constant in eqn (15), since diffusion occurs from both sides. Thus, the time constant for symmetrical samples corresponds to

$$\tau_{\mathrm{s}} = \tau/4. \tag{16}$$

Warburg elements

The impedance of diffusion processes has traditionally been accounted for in equivalent circuits by so-called Warburg elements. These circuit elements consider concentration gradients as the only driving force for mass transport. Thus, electrical potential gradients are neglected and eqn (1) is reduced to Fick's first law of diffusion, which can then be solved analytically for the

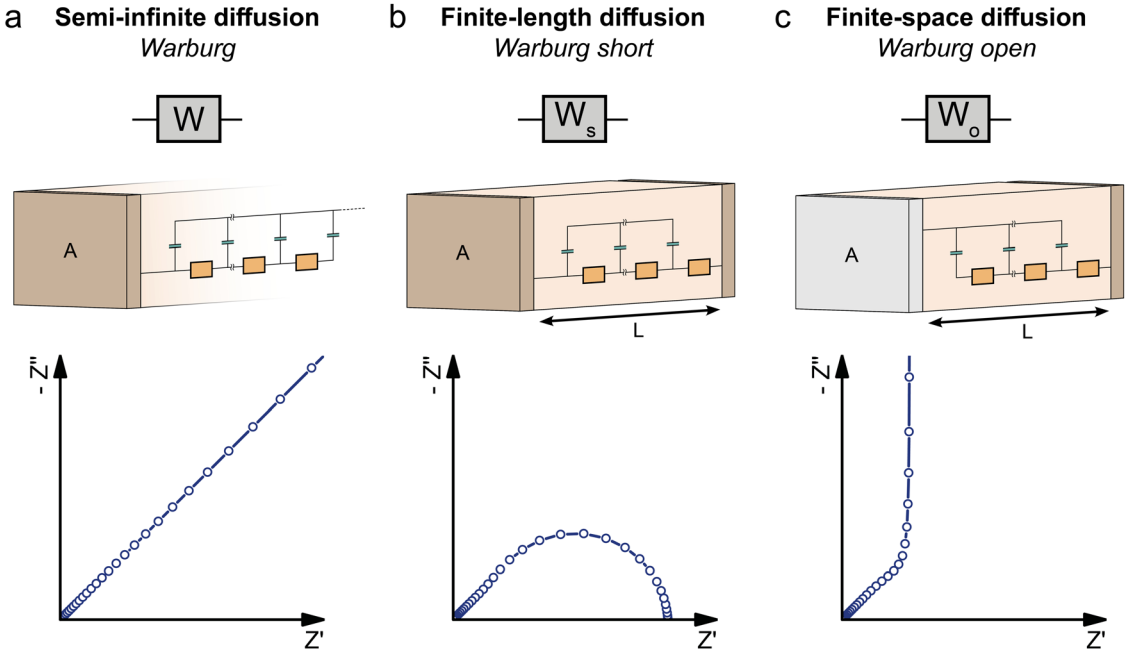

Fig. 2 Different Warburg elements, their equivalent transmission lines, and their impedance responses, describing the impedance of concentration-driven diffusion for different boundary conditions. (a) Semi-infinite diffusion (Warburg). (b) Finite-length diffusion (Warburg short). (c) Finite-space diffusion (Warburg open).

appropriate boundary conditions and expressed as a current density to derive an impedance expression.

In the transmission line picture, the Warburg impedance is a special case where one charge carrier has negligible resistance, and all terminal impedances are either short or open circuits. By variation of the boundary conditions, three different cases result: semi-infinite diffusion, finite-length diffusion and finite-space diffusion. In the following, we briefly summarize the three different Warburg elements, their impedance expressions and their equivalent circuit forms.

Semi-infinite diffusion considers the diffusion of particles from an infinite distance towards a transmissive boundary. In practice, this means that the sample thickness is large enough, or the diffusional resistance is high enough, for spatial limitations not to become relevant within the low-end frequency range of the impedance measurement. The corresponding impedance expression can be derived as[19]

$$Z_{\mathrm{W}} = \frac{S_{\mathrm{W}}}{\sqrt{\omega}} - i\frac{S_{\mathrm{W}}}{\sqrt{\omega}}, \tag{17}$$

with the Warburg coefficient S_{W} (see below). The impedance response of semi-infinite diffusion is characterized by a constant -45° phase shift, resulting in a straight line at an angle of 45° in a Nyquist plot, as shown in Fig. 2a, down to the lowest frequencies. As a result, the Warburg impedance can also be written as a constant-phase element (CPE) according to

$$Z_{\mathrm{CPE}} = \frac{1}{(i\omega)^{\alpha}Q}, \tag{18}$$

with $\alpha = 1/2$ and

$$Q = \left(S_{\mathrm{W}}\sqrt{2}\right)^{-1}, \tag{19}$$

with Q containing differential resistive (r, real) and capacitive (c, imaginary) impedance contributions. More explicitly, such a constant phase element can be expressed as a semi-infinite transmission line of differential resistors r and capacitors c, as shown in Fig. 2a, with

$$Z_{\mathrm{W}} = \sqrt{\frac{r}{i\omega c}} \tag{20}$$

and thus (*cf.* telegraph equations)

$$Q = \sqrt{\frac{c}{r}}. \tag{21}$$

The Warburg impedance is not specific to ion diffusion in a solid, but common to a wide range of diffusion processes, including gaseous diffusion of neutral O_2 towards an absorbing boundary or pore diffusion of Li^+ through a porous LIB electrode. Although the general form of the impedance expressions and transmission line is the same for all cases of semi-infinite diffusion, the physical meaning of the capacitors and resistors depends on the specific context. For example, for the case of concentration-driven ion diffusion through an MIEC ($R_{\mathrm{eon}} \approx 0$), we can identify the circuit elements of the transmission line as the incremental ionic resistances r_{ion} and chemical capacitances c_{chem} by comparison to Fig. 1a. Using eqn (13), (14), (20), and (21), the Warburg coefficient for area A can then be

expressed as

$$S_W = \frac{1}{\sqrt{2C^V_{chem}\sigma_{ion}}} \cdot \frac{1}{A}, \quad (22)$$

and the parameter Q is given by

$$Q = \sqrt{C^V_{chem}\sigma_{ion}} \cdot A. \quad (23)$$

Both the resistive and capacitive contributions to Z_W are frequency-dependent for the entire frequency range.

When the sample is thin enough, or the diffusional resistance low enough, for spatial limitations to become relevant within the low-end frequency range of the impedance measurement, boundary conditions need to be considered for both sides of the sample. For the case that both boundaries are fully transmissive for the diffusing species, the limiting impedance for $\omega \to 0$ is real and corresponds to the total diffusional resistance R (*e.g.* $R = R_{ion}$ for concentration-driven ion diffusion through an MIEC with $R_{eon} \approx 0$). Thus, in the low-frequency limit, the impedance is independent of frequency. This situation is often referred to as finite-length diffusion (see Fig. 2b), and for diffusing ions its frequency-dependent impedance response is given by

$$Z_{W_s} = R_{ion}\frac{\tanh\sqrt{i\omega\tau_s}}{\sqrt{i\omega\tau_s}}. \quad (24)$$

The corresponding Warburg element is labelled Warburg short (W_s) and is equivalent to the transmission line shown in Fig. 2b.[19]

If only one boundary is transmissive for the diffusing particles and the other blocks mass transport, the limiting impedance for $\omega \to 0$ is purely capacitive with a real offset corresponding to $R_{ion}/3$ (for $R_{eon} \approx 0$) meaning that only the capacitive part of the impedance is frequency dependent in the low-frequency limit.[11] This situation is referred to as finite-space diffusion and for diffusing ions results in the impedance expression

$$Z_{W_o} = R_{ion}\frac{\coth\sqrt{i\omega\tau}}{\sqrt{i\omega\tau}}. \quad (25)$$

The corresponding equivalent circuit element is labelled Warburg open (W_o), and its transmission line representation is shown in Fig. 2c.[19] In contrast to W, W_s and W_o allow the simultaneous extraction of the resistive and capacitive transport properties from impedance spectra, due to their different frequency-dependences at low-frequencies.[11]

In the following, the general transmission line from Fig. 1a will be applied to a variety of different measurement setups involving MIECs and electrolytes. Wherever appropriate, references will be made to the Warburg elements presented above, highlighting their relation to the general MIEC transmission line, but also their limitations.

Symmetrical measurements

Symmetrical impedance measurements on electrolytes and MIECs constitute the simplest class of measurements that can be rationalized from a transmission line perspective. For their interpretation, it is usually enough to consider the analytical expression given by Lai and Haile for a symmetrical transmission line with $Z_A = Z_C$ and $Z_B = Z_D$,[9] which is less cumbersome than the general expression for four different terminals.

Ion-blocking contacts on electrolytes

First, let us consider symmetrical impedance measurements on ideal electrolytes with negligible electronic conductivity in the context of the general MIEC transmission line model. Such measurements often use purely electron conducting contacts and their main purpose is the characterisation of an electrolyte's ionic conductivity. Typical experimental setups include in-plane[20–23] and cross-plane[24,25] measurements on thin films, bulk single crystals and polycrystals.[26–28] In either case, we consider a slab of electrolyte sandwiched between two identical electronically conducting contacts.

Due to the negligible electronic conductivity of the electrolyte ($R_{eon} \to \infty$), the electronic rail of the transmission line model in Fig. 1a can be discarded including its terminal elements, and thus also C_{chem} is negligible. The remaining circuit is shown in Fig. 3a. This approach to the equivalent circuit also emphasizes that the only way ions can lead to a DC current is *via* coupling reaction resistances R_{react}. If the contacts present a completely blocking boundary to ions from the electrolyte, this coupling resistance on the ionic rail becomes infinitely large ($R_{react} \to \infty$), leaving only the interfacial capacitances $C_{e/i}$ at the contact interfaces. Experimentally, this is (approximately) realized, for example, when contacting a sample of a Li^+ solid electrolyte such as lithium phosphorous oxynitride (LiPON) with two Ti electrodes, as shown schematically in Fig. 3b. Assuming two identical Ti contacts, the transmission line is thus reduced to a simple equivalent circuit consisting only of C_{diel} in parallel to a serial connection of R_{ion} and the total interfacial capacitance $C_{int} = C_{e/i}/2$ as shown in Fig. 3b.

Since dielectric capacitances are typically much lower than interfacial capacitances ($C_{diel} \ll C_{int}$), the resulting impedance response ideally consists of a high-frequency bulk semicircle ($R_{ion}|C_{diel}$) which transitions into purely capacitive behaviour ($R_{ion} + C_{int}$) at lower frequencies. In consequence, the quality of separation between these two regimes depends on the relative magnitudes of C_{diel} and C_{int}. The former often also contains stray capacitances from the experimental setup (for example, from the substrate in in-plane measurements on a thin film) and C_{diel} can therefore deviate from the bulk dielectric capacitance of the electrolyte.[20,23] Further deviations from the ideal impedance spectrum in Fig. 3b can arise from imperfect ion blockage by the contacts (*i.e.* finite R_{react}).[26] Since the high-frequency semicircle corresponds to the bulk impedance response of the electrolyte (or MIEC), it is commonly referred to as the bulk semicircle.

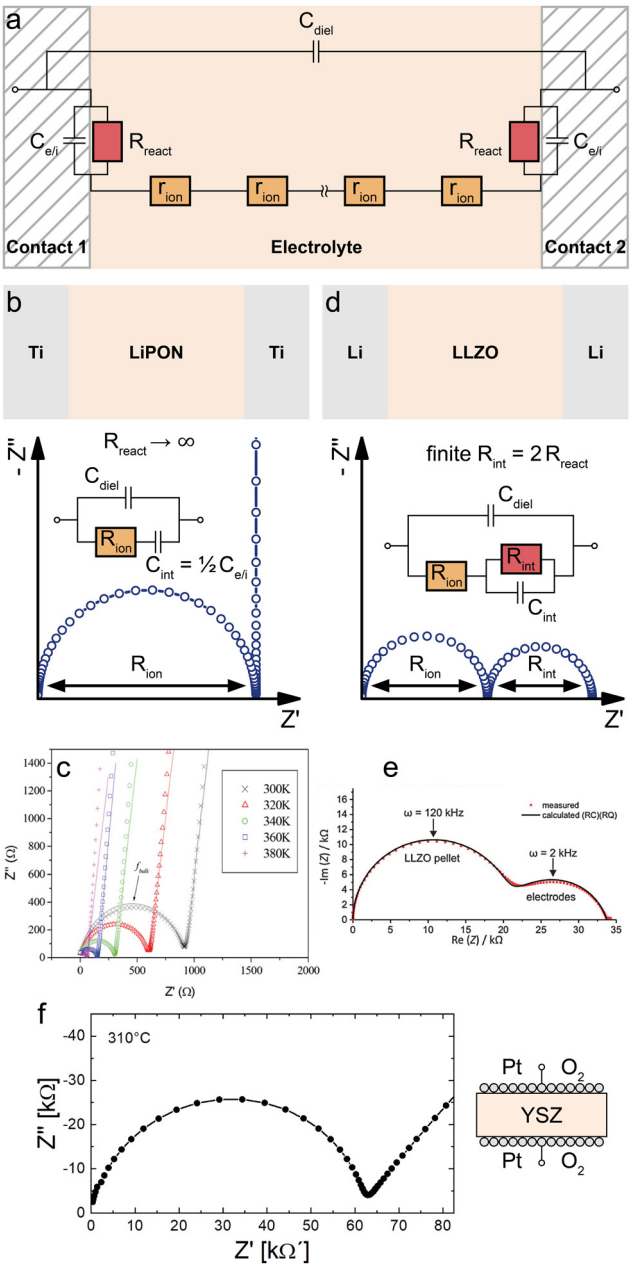

Fig. 3 (a) Adapted transmission line for an ideal ionic conductor (electrolyte) between two identical contacts. (b) Schematic sketch, equivalent circuit and simulated impedance response of LiPON between two ideal (ion-blocking, R_B,$R_D \rightarrow \infty$) Ti contacts. The impedance spectrum consists of a high-frequency semicircle ($R_{ion}|C_{diel}$) and a capacitive line at low frequencies. (c) Measured impedance of a symmetrical Ti|LiPON|Ti thin film sample. Image reprinted from ref. 29 with permission from Elsevier. (d) Schematic sketch, equivalent circuit and simulated impedance response of LLZO between two Li contacts. The impedance spectrum consists of two semicircles corresponding to $R_{ion}|C_{diel}$ and $R_{int}|C_{int}$. (e) Measured impedance of an LLZO pellet contacted by two Li electrodes. Image reprinted (adapted) from ref. 30 with permission from RSC Publishing. (f) Measured impedance of a YSZ pellet contacted by two LSC thin film electrodes covered with Pt paste. Diagram reproduced using data from ref. 26. A sample sketch was added for clarity.

For example, Fig. 3c shows the temperature-dependent cross-plane impedance response of a LiPON thin film sandwiched between two ion-blocking Ti electrodes, taken from ref. 29. The impedance spectra are very close to the ideal behaviour expected from Fig. 3b, with a bulk semicircle followed by a nearly vertical line due to the blocking interfacial capacitance of the contacts. The minor slope of the capacitive line can be accounted for by replacing the corresponding capacitance in the equivalent circuit by a constant-phase element, which allows for a more accurate fit of the bulk semicircle, especially in cases where the two features are not as well separated as in Fig. 3c.

If the contacts are partially transmissive for ions, the finite terminal resistances R_{react} on the ionic rail in Fig. 3a have to be taken into account together with the corresponding interfacial capacitance $C_{e/i}$. Accordingly, we get the total interfacial capacitance $C_{int} = \frac{1}{2}C_{e/i}$ and the total interfacial resistance $R_{int} = 2R_{react}$. The resulting equivalent circuit exhibits a similar impedance response as two serial $R|C$ elements as long as the corresponding time constants are well separated, as shown in Fig. 3d. Experimentally, this situation can be realized by sandwiching an electrolyte between two reservoir electrodes that enable the required electrochemical reaction which couples the ionic to the electronic rail. In the context of LIB solid electrolytes, Li metal or a LiAl alloy are commonly used as the reservoir electrode, enabling the reaction $Li^+ + e^- \rightleftharpoons Li$. (Please note that in the alloying case, R_{react} may not be sufficient for describing the relevant processes since diffusion in the alloy also comes into play.)

For example, Fig. 3e shows the impedance response of an Al-doped $Li_7La_3Zr_2O_{12}$ (LLZO) polycrystalline pellet with two symmetrical Li contacts, taken from ref. 30. As indicated in the figure, the high- and low-frequency semicircles correspond to the LLZO bulk ($\sim R_{ion}|C_{diel}$) and Li electrodes ($\sim R_{int}|C_{int}$) respectively, where R_{int} corresponds to the charge-transfer resistances at the two Li/LLZO interfaces.

For O^{2-} electrolytes, on the other hand, contacts enabling oxygen exchange (*e.g. via* $1/2O_2 + 2e^- \rightleftharpoons O^{2-}$) are required, *e.g.* porous Pt electrodes. Fig. 3f shows the example of an yttria-stabilized zirconia (YSZ) single crystal symmetrically contacted by Pt paste electrodes, taken from ref. 26. This leads to a bulk semicircle ($\sim R_{ion}|C_{diel}$) at high frequencies and an electrode feature at low frequencies. In this case, however, the high- as well as the low-frequency feature is far from an ideal semicircle and thus constant phase elements are required for an appropriate fit. Please note that on oxide ion conductors often mixed conducting electrodes are used, which may further complicate the terminal impedances. For measurements on polycrystals, an additional impedance feature due to grain boundaries is often found, which is not considered by the transmission line in Fig. 3a. For a more detailed discussion of the impedance contribution of grain boundaries, the interested reader is referred to the specialized literature.[20,31–33]

Ion-blocking contacts on MIECs

If the electronic and ionic conductivities are both significant, the material classifies as an MIEC. A determination of the corresponding material parameters in the transmission line (σ_{eon}, σ_{ion}, C_{chem}) is then often based on measurements using

the symmetrical cells shown in Fig. 1d and e, with further specified terminal elements Z_A and Z_B. Let us first consider the case of electron conducting contacts. Ideally, the charge transfer resistance of the electrons is negligible, $R_{ct,e} \rightarrow 0$, while the electrodes are completely blocking for ions, $R_{react} \rightarrow \infty$, as sketched in Fig. 4a. Then, the terminal impedance Z_A is negligible and Z_B reduces to the interfacial capacitance $C_{e/i}$ (Fig. 4b). Even for a finite $R_{ct,e}$ the corresponding parallel capacitance $C_{e/e}$ is often neglected, since it leads to an over-parameterisation of the impedance fit.

The shape of the resulting impedance spectrum strongly depends on the relative magnitudes of σ_{eon} *versus* σ_{ion} and C_{chem} *versus* $C_{e/i}$, as well as on the portion of the impedance response that is accessible within commonly measured frequency ranges. Please note that the following discussion in terms of $\sigma_{ion}/\sigma_{eon}$ and $C_{e/i}/C_{chem}$ is equivalent to the viewpoint of carrier mobilities and concentrations adopted in ref. 13 (Fig. 7), since these are related *via* eqn (5) and (6).

Electronic charge carrier mobilities are typically much higher than for ionic carriers, and thus many MIECs are predominantly electronic conductors, such that $\sigma_{ion} \ll \sigma_{eon}$ applies. Examples of such materials include many LIB and SOFC cathode materials such as LCO, $LiMn_2O_4$ (LMO), LSF or LSC.[5,7,8,40,41] In some cases, both conductivities are of a similar magnitude ($\sigma_{eon} \approx \sigma_{ion}$), for example, in heavily Tb-doped YSZ,[42] or $Sr(Ti,Fe)O_{3-\delta}$ (STF).[43] Examples of MIECs with predominant ionic conductivity are mostly encountered in the context of non-ideal electrolytes, such as partially reduced LLTO or GDC,[44,45] and often limited to certain stoichiometric regions. An example of an insertion electrode material with predominant ionic conductivity is stoichiometric $Na_3V_2(PO_4)_2F_3$ (NVPF),[36,46] a cathode material for Na-ion batteries.

For MIECs with similar ionic and electronic conductivities such as highly Fe-doped STF at low pO_2,[35,43] the impedance response of the transmission line in Fig. 4b consists of two separate features that allow a simultaneous extraction of σ_{ion} and σ_{eon}, as shown in Fig. 4e and f. The high-frequency semicircle corresponds to the bulk response of the mixed conductor, with the dielectric capacitance coupled to the effective bulk resistance R_{bulk}, which is related to the total conductivity $\sigma_{tot} = \sigma_{ion} + \sigma_{eon}$ according to

$$R_{bulk} = \left(R_{ion}^{-1} + R_{eon}^{-1}\right)^{-1} = \frac{L}{\sigma_{tot} A}. \quad (26)$$

Thus, R_{bulk} behaves like a parallel connection of R_{ion} and R_{eon}, being mostly defined by the smaller of the two resistances. Due to its typically small time constant $\tau_{bulk} \approx R_{bulk}C_{diel}$ relative to the frequency range of the measurement, the bulk semicircle may not be fully visible in the impedance spectrum. Generally, its accessibility is favoured by low temperatures, which increase the value of τ_{bulk}. The low-frequency impedance feature, on the other hand, is due to the selective charge carrier blocking at the contact interfaces and approaches the transport resistance of the non-blocked carrier, in this case R_{eon}, for $\omega \rightarrow 0$. Qualitatively, the relative values of σ_{ion} and σ_{eon} can therefore be visually estimated from the relative magnitudes of the two impedance features. The resistance associated with the low-frequency feature ($R_{eon} - R_{bulk}$) indicates how much the conductivity of the blocked carriers, in this case ions, contributes to $\tilde{\sigma}$. Thus, for ion-blocking contacts, a comparatively large low-frequency feature signifies $\sigma_{ion} > \sigma_{eon}$ and *vice versa*. The shape of the low-frequency feature may vary continuously between an ideal semicircle and a half-teardrop shaped Warburg feature, depending on the relative magnitudes of $C_{e/i}$ and C_{chem}. For a relatively high chemical capacitance $C_{e/i} \ll C_{chem}$, the low-frequency feature is identical to a finite-length Warburg element (Warburg short, *cf.* Fig. 2b) with a resistance $R_{W_s} = R_{eon} - R_{bulk}$. This equivalence can also be shown mathematically by applying $C_{e/i} = 0$ (and $R_{ct,e} = 0$) to the analytical impedance expression corresponding to the transmission line in Fig. 4b (see ref. 9, eqn (73)). Thus, the equivalent circuit can be further simplified into a serial connection of R_{bulk} and W_s parallel to C_{diel}.

Such a circuit was applied, for example, in ref. 35, where the in-plane impedance of STF thin films on MgO was studied under reducing conditions using interdigitated Pt microelectrodes, as shown in Fig. 4j. Only the onset of the bulk semicircle can be seen at the highest frequencies, which transitions into the half-teardrop shape corresponding to W_s. Both features are of similar size, indicating very similar electronic and ionic conductivities of the material. Furthermore, the two features are well separated, allowing a further simplification of the circuit by neglecting the dielectric capacitance ($C_{diel} = 0$) and treating the bulk semicircle as a high-frequency offset R_{bulk}. This way, σ_{eon}, σ_{ion}, and C_{chem} could be extracted from the impedance data without having to implement a fit to the full transmission line.

For significantly different σ_{ion} and σ_{eon}, the impedance spectrum is dominated either by the bulk semicircle ($\sigma_{ion} \ll \sigma_{eon}$) or the low-frequency feature ($\sigma_{ion} \gg \sigma_{eon}$). If both features are sufficiently resolved within the measured frequency range, the spectrum can be fitted using the full transmission line in Fig. 4b, or even the simplified circuit in Fig. 4e for $C_{int} \ll C_{chem}$, to obtain all three bulk properties (σ_{eon}, σ_{ion}, and C_{chem}).

For example, in ref. 37, the cross-plane impedance of 2% Fe-doped $SrTiO_3$ (Fe:STO) thin films on Nb-doped $SrTiO_3$ (Nb:STO) single crystals was studied using Pt microelectrodes (see Fig. 4l). The resulting impedance spectrum consists of a depressed low-frequency semicircle (apex frequency 358 Hz) and a significantly smaller high-frequency arc. By comparing the corresponding capacitances with the dielectric capacitance expected for the Fe:STO thin film, the high-frequency arc could be identified as the bulk semicircle originating from R_{bulk} coupled to C_{diel}. Since the low-frequency feature does not exhibit a well-defined W_s behaviour, but is closer in shape to a semicircle, a fit of the full transmission line ($R_{ct,e} = 0$) had to be applied, implying $C_{e/i} > C_{chem}$. In fact, the fit shown in Fig. 4l yields a value of $C_{e/i}$ that is approximately one order of magnitude larger than C_{chem}, as can be deduced from the corresponding fit parameters given in the ESI of ref. 37. Please note that in this example, the interfacial capacitances were fitted as constant phase elements, and the values of $C_{e/i}$ can only be estimated by converting the non-physical fit parameters

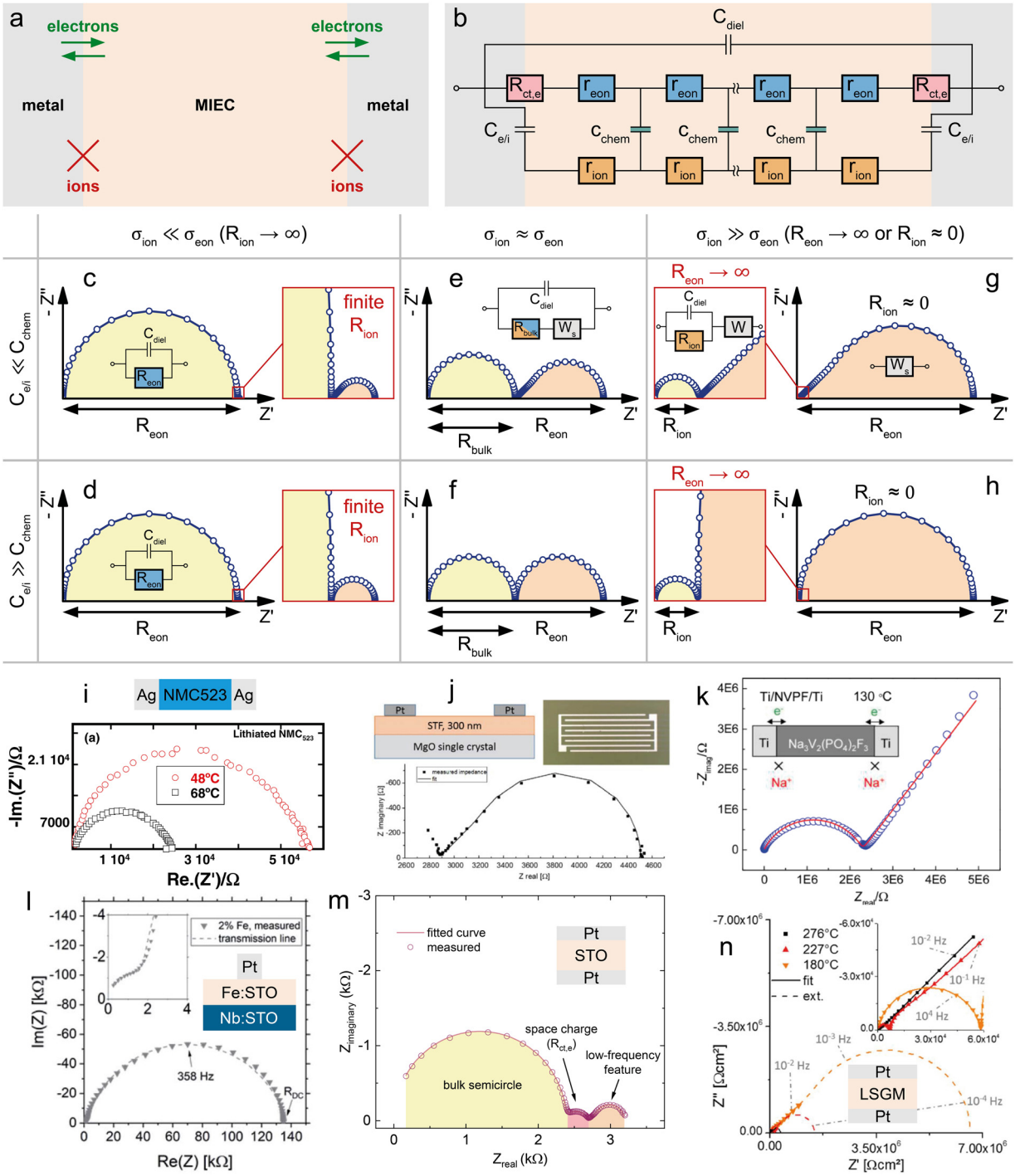

Fig. 4 (a) Schematic sketch of a mixed ionic and electronic conductor between two ideal (ion-blocking) metal contacts. (b) Adapted transmission line corresponding to the sample sketch in subfigure (b). (c)–(h) Simulated impedance responses of the above transmission line circuit for different relative magnitudes of $C_{e/i}$ *versus* C_{chem} and σ_{ion} *versus* σ_{eon}. (i) Temperature-dependent impedance spectrum of an NMC523 pellet between two ion-blocking Ag contacts. Original image published in ref. 34 under a CC BY-NC-ND license. (j) In-plane impedance of an STF thin film under reducing conditions measured between two interdigitated Pt contacts. Original image published in ref. 35 under a CC BY license. (k) Measured impedance response of an NVPF pellet between two Ti contacts. Image reprinted (adapted) from ref. 36 with permission from ACS Publications. (l) Impedance spectrum of an Fe:STO thin film between a Nb:STO substrate and a Pt top contact. Original image published in ref. 37 under a CC BY license. (m) Impedance response of an STO single crystal between two Pt contacts. Diagram reproduced using data from ref. 38. (n) Temperature-dependent impedance response of an LSGM single crystal between two Pt contacts. Original image published in ref. 39 under a CC BY license. For subfigures (i), (l), (m), and (n), sample sketches were added for clarity.

Q and n into a corresponding capacitance (see, for example, ref. 31 eqn (15)). As expected from the dominance of the low-frequency impedance feature, the Fe:STO thin film sample is a predominant ionic conductor, with σ_{ion} being about two orders of magnitude higher than σ_{eon}. Thus, according to eqn (26), the effective bulk resistance R_{bulk}, which corresponds to the high-frequency arc, is virtually identical to R_{ion}. At high frequencies, the predominant ionic conductor therefore behaves like an electrolyte (*cf.* Fig. 3b), with $R_{eon} \to \infty$, as shown in the inset of Fig. 4h. On the other hand, the resistance associated with the low-frequency feature can then be approximated by $R_{eon} - R_{bulk} \approx R_{eon} - R_{ion} \approx R_{eon}$. If either of the two impedance features is not sufficiently resolved to perform a reliable transmission-line fit, these approximations may be used to obtain either σ_{ion} or σ_{eon}.

A very illustrative example is also given by Rupp *et al.* in ref. 39, where the temperature-dependent impedance of $La_{0.95}Sr_{0.05}Ga_{0.95}Mg_{0.05}O_{3-\delta}$ (LSGM) single crystals is measured in synthetic air using symmetrical Pt contacts, as shown in Fig. 4n. The impedance response generally consists of a dominant W_s feature at low frequencies, indicating predominant ionic conductivity ($\sigma_{ion} \gg \sigma_{eon}$) together with a comparatively large chemical capacitance ($C_{e/i} \ll C_{chem}$), and a much smaller bulk semicircle at high frequencies. The former and latter are only visible at high and low temperatures, respectively. Upon closer inspection, the 45° onset of the W_s feature contains an additional semicircle, which the authors attribute to a non-negligible electronic charge transfer resistance, terminating the electronic rail at the Pt|LSGM interface. In the transmission line in Fig. 4b, this corresponds to leaving two finite terminal resistances $R_A = R_C = R_{ct,e}$ at the electronic rail ends (*cf.* Fig. 1b, without corresponding capacitances $C_{e,e}$ to avoid overparameterisation). Apart from the small $R_{ct,e}$, the measured impedance response closely matches the simulated spectrum shown in Fig. 4g. At high temperatures (see ref. 39 for details), all time constants decrease, such that the low-frequency feature is fully contained in the measured frequency range (1 MHz to 5 mHz), but the bulk semicircle is beyond the high-frequency limit. Thus, the effective bulk resistance R_{bulk} is treated as a high-frequency offset and C_{diel} is neglected. Since the electronic charge transfer semicircle is negligible at high temperatures, the spectra are fitted to a simple $R_{bulk} + W_s$ circuit. At low temperatures (Fig. 4n), on the other hand, the bulk semicircle is fully visible, while only part of the 45° region of the Warburg feature is contained in the measured spectrum. Also, the charge transfer semicircle at mid frequencies is significant at low temperatures. As a consequence, these impedance spectra were fitted using the full transmission line from Fig. 4b, including $R_A = R_C = R_{ct,e}$. However, since the low-frequency Warburg feature is not fully contained in the data, the corresponding fitting errors for R_{eon} and C_{chem} exceed 100%.

The presence of such a non-negligible interfacial resistance $R_{ct,e}$ is even more evident in ref. 38, where the impedance of an STO single crystal between to Pt contacts is analysed. An exemplary spectrum, measured at a temperature of 600 °C and an oxygen partial pressure of 7×10^{-7} bar, is shown in Fig. 4m. Under these conditions, STO is a mixed conductor with σ_{ion} similar to σ_{eon}, which is evident as the resistances associated with the high-frequency bulk and low-frequency W_s features are roughly within the same order of magnitude. In the mid-frequency range, an additional semicircle is clearly visible, which the authors attribute to a space charge resistance ($R_{s.c.} = R_{ct,e}$) at the Pt/STO interfaces. Just like in the previous example of LSGM, the entire impedance spectrum with three arcs could therefore be fitted using a single transmission line (Fig. 4b), yielding an excellent quality of fit and physically meaningful material parameters.

An alternative approach to fitting a spectrum with a curtailed low-frequency Warburg feature, such as the one in Fig. 4n, is given in ref. 36. There, the mixed conductivity of the Na intercalation material NVPF is investigated by means of impedance spectroscopy using symmetrical Ti electrodes on a polycrystalline NVPF pellet, as shown in Fig. 4k. The resulting impedance response resembles that of the inset in Fig. 4g ($C_{e/i} \ll C_{chem}$), with a high-frequency bulk semicircle ($R_{bulk}|C_{diel}$) and a low-frequency 45° onset. Just like in the previous example of Pt|LSGM|Pt at low temperatures (Fig. 4m right), the full bulk semicircle is visible in the high-frequency region, while only the 45° portion of the low-frequency feature is contained in the measured data. Thus, it is not possible to perform a fit that yields reliable values for both σ_{ion} and σ_{eon}. However, the dominant Warburg response at low frequencies indicates $\sigma_{ion} \gg \sigma_{eon}$, meaning that the bulk resistance associated with the high-frequency semicircle can be approximated as $R_{bulk} \approx R_{ion}$ according to eqn (26). Thus, the ionic conductivity was obtained by fitting the spectrum with a simple $R_{ion}|C_{diel} + W$ circuit, as shown in Fig. 4g. In this case, the fit parameters related to the semi-infinite Warburg element W are not further evaluated.

Finally, we consider the case of a predominant electronic conductor with $\sigma_{ion} \ll \sigma_{eon}$. The transmission line in Fig. 4b ($R_{ct,e} = 0$) can then be simplified further by assuming $R_{ion} \to \infty$, resulting in a simple $R_{eon}|C_{diel}$ circuit with a corresponding semicircle in the Nyquist plot (Fig. 4c and d). For example, in ref. 34 the impedance of a sintered pellet of $LiNi_{0.5}Mn_{0.2}Co_{0.3}O_2$ (NMC523) was measured for symmetrical silver contacts (Ag|NMC523|Ag) below 100 °C. The corresponding impedance spectra at two different temperatures are shown in Fig. 4i and exhibit the expected shape of a non-ideal semicircle, which is fitted using a $R_{eon}|Q_{diel}$ circuit to obtain the electronic conductivity. Again, the calculated impedance spectra in Fig. 4c and d principally consist of a high-frequency bulk semicircle, which is dominant for $\sigma_{ion} \ll \sigma_{eon}$, and a much smaller low-frequency feature, with a shape depending on the relative magnitudes of $C_{e/i}$ and C_{chem}. However, due to the comparatively small resistance associated with this feature, it is often not visible in real impedance spectra, as in Fig. 4i.

Electron-blocking contacts on MIECs

Symmetrical impedance measurements with two electron-blocking contacts are experimentally much more challenging and therefore less common. Usually, such setups consist of a central MIEC sample to be characterized, sandwiched between a double layer of an ion conductor (inner layer = electron-

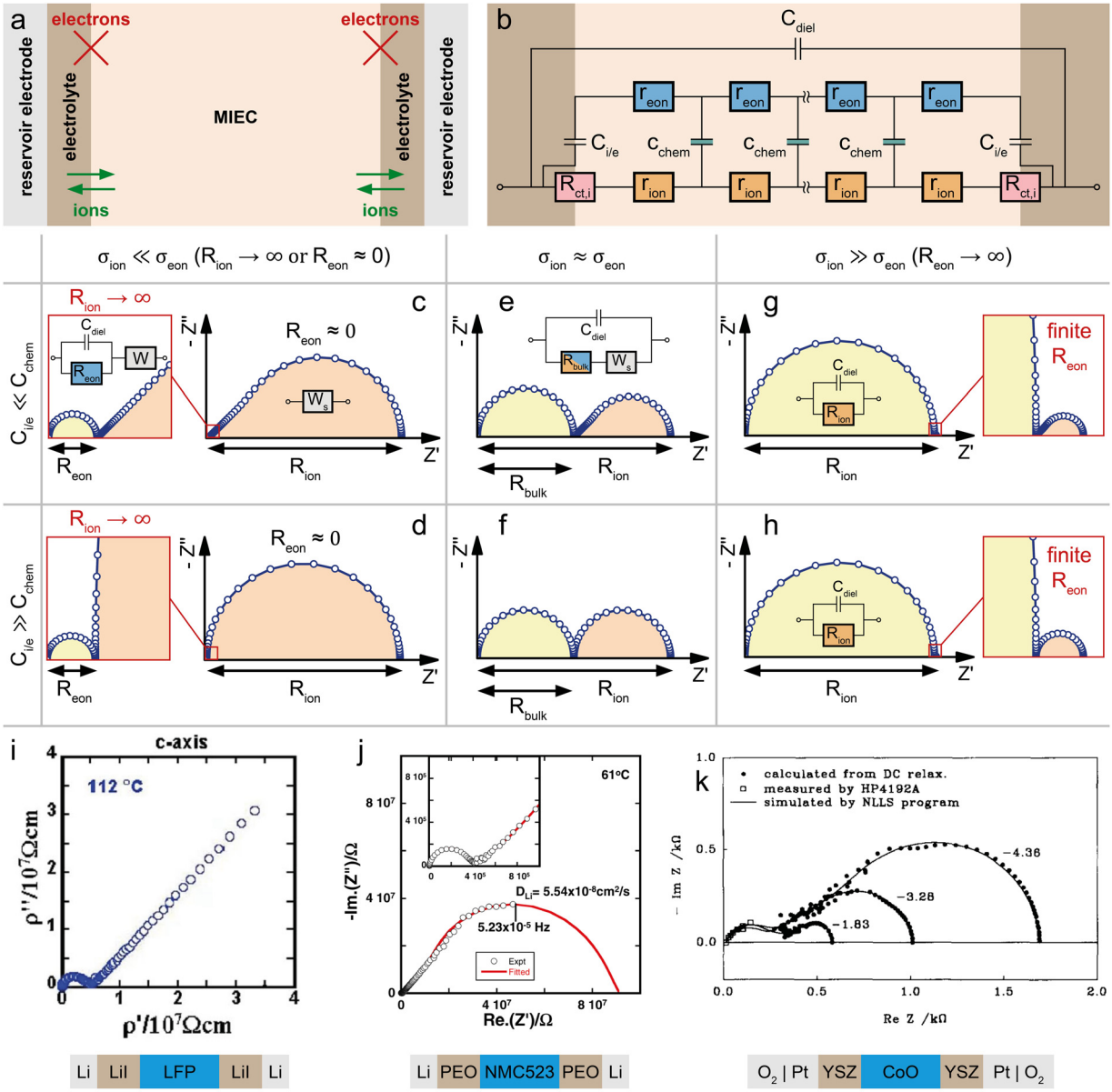

Fig. 5 (a) Schematic sketch of a mixed ionic and electronic conductor between two ideal (electron-blocking) ion-conducting contacts. Reservoir electrodes are required to provide a contact to the external circuit. (b) Adapted transmission line corresponding to the sample sketch in subfigure (b), neglecting the outer reservoir electrodes. (c)–(h) Simulated impedance responses of the above transmission line circuit for different relative magnitudes of $C_{e/i}$ *versus* C_{chem} and σ_{ion} *versus* σ_{eon}. (i) Impedance response of a Li|LiI|LFP|LiI|Li cell, with a *c*-axis oriented LFP single crystal. Image reprinted from ref. 47 with permission from IOP Publishing. (j) Impedance response of a Li|PEO|NMC523|PEO|Li cell, with a sintered NMC523 pellet. Original image published in ref. 34 under a CC BY-NC-ND license. (k) Impedance response of a O_2|Pt|YSZ|CoO|YSZ|Pt|O_2 cell. In the low-frequency range, the data was obtained from DC relaxation measurements. Image reprinted from ref. 48 with permission from Elsevier. For subfigures (i)–(k), sample sketches were added for clarity.

blocking layer) and a reversible reservoir electrode (outer layer), as shown in Fig. 5a. The reservoir electrode acts as an elemental source and sink and is therefore required to be a low-impedance electrode such as Li metal or a reversible mixed conducting O_2 electrode in the case of Li^+ materials and SOFC materials, respectively. In other words, the reservoir electrode couples the ionic current across the electron-blocking layer and MIEC to the electronic current in the external circuit *via* an electrochemical reaction. Not surprisingly, this coupling reaction as well as mass and charge transport across the reservoir/electrolyte/MIEC interfaces is usually associated with non-negligible resistances, which contribute to the complexity of the measured impedance spectra. An additional resistance may arise from the finite ionic bulk conductivity of the electrolyte. Although all these contributions could be explicitly considered in the equivalent circuit, overlaps of the corresponding impedance features often limit their interpretability. Nonetheless, measurements on electron-blocking cells are an important

complementary tool that can yield valuable, albeit often incomplete, information about the ambipolar conductivity of MIECs. In particular, the otherwise elusive ionic conductivity of predominant electronic conductors, such as most LIB cathode materials, can become accessible by this method.

To understand the impedance response of the isolated electrolyte/MIEC/electrolyte cell, we start from the circuit of the symmetrical cells with ionic contacts in Fig. 1e. For complete electron blocking ($R_{react} \rightarrow \infty$) and a negligible ionic charge transfer resistance ($R_{ct,i} \rightarrow 0$), we end up with only one terminal element remaining, namely the coupling capacitance $C_{i/e}$. The resulting circuit is shown in Fig. 5b and is electrically equivalent to that for ion-blocking contacts in Fig. 4b.

As a result, also the calculated impedance response is inverted with respect to R_{ion} and R_{eon}, which becomes obvious when comparing the simulated spectra in Fig. 4 and 5. Just like for ion-blocking contacts, the impedance spectrum for a mixed conductor ($\sigma_{ion} \approx \sigma_{eon}$) consists of a high-frequency bulk semicircle and a low-frequency feature that takes the shape of either a W_s element ($C_{i/e} \ll C_{chem}$) or a semicircle ($C_{i/e} \gg C_{chem}$), as shown in Fig. 5e and f. While the bulk semicircle is still related to the effective bulk resistance R_{bulk}, the limiting DC resistance for $\omega \rightarrow 0$ is now given by R_{ion}, such that the low-frequency feature is associated with a resistance $R_{ion} - R_{bulk}$. In contrast to ion-blocking contacts, it is now the low-frequency feature that dominates the spectrum for predominant electronic conductors ($\sigma_{ion} \ll \sigma_{eon}$), since it indicates how much the blocked charge carriers (in this case electrons) contribute to the total conductivity. Its resistance can be approximated as R_{ion}, while the much smaller bulk resistance is virtually identical to R_{eon} (see Fig. 5c and d). For a predominant ionic conductor with $\sigma_{ion} \gg \sigma_{eon}$, on the other hand, the spectrum consists of a large bulk semicircle ($\sim R_{ion}|C_{diel}$) and a much smaller low-frequency feature (see Fig. 5g and h).

For example, in ref. 47, the anisotropic electronic and ionic conductivity of $LiFePO_4$ (LFP) single crystals is investigated by electron-blocking impedance measurements in a symmetrical Li/LiI/LFP/LiI/Li arrangement. A typical spectrum measured along the crystallographic *c*-axis at 112 °C is shown in Fig. 5i, consisting of a high-frequency semicircle and an extended 45° Warburg response at low frequencies, suggesting $C_{i,e} \ll C_{chem}$. Although the low-frequency region is not fully contained in the spectrum, its associated resistance is apparently much larger than the semicircle, indicating $\sigma_{ion} \ll \sigma_{eon}$. The bulk resistance can therefore be approximated as $R_{bulk} = R_{eon}$, with $R_{ion} \rightarrow \infty$, as shown in the inset of Fig. 5c, and the electronic conductivity can be extracted from the high-frequency semicircle. In that sense, the present example is fully analogous to the impedance spectrum of NVPF in Fig. 4k (ref. 36) measured with ion-blocking contacts. Importantly, however, the authors of ref. 47 note that the semicircle in Fig. 5i also contains ionic contact ("charge transfer") impedances and minor contributions from the bulk conductivity of the electrolyte (LiI). Thus, the extracted values of σ_{eon} differ slightly from those obtained from measurements with ion-blocking metal contacts, highlighting the experimental difficulties associated with electron-blocking configurations.

A similar example is given in ref. 34, where the impedance of a sintered $LiNi_{1/3}Mn_{1/3}Co_{1/3}O_2$ (NMC111) pellet is measured in a symmetrical setup using doped polyethylene oxide (PEO) as the electrolyte (electron-blocking layer) and Li metal as the outer reservoir electrode. The resulting impedance spectrum at 61 °C is shown in Fig. 5j, again exhibiting a small high-frequency semicircle and a low-frequency Warburg response. In this case however, enough of the low-frequency region is contained in the spectrum to fit it as a W_s element with an associated resistance $R_{W_s} = R_{ion} - R_{bulk}$, which the authors approximate as $R_{W_s} \approx R_{ion}$ due to $\sigma_{ion} \ll \sigma_{eon}$ (and thus $R_{bulk} \ll R_{ion}$) to extract the Li diffusivity and ionic conductivity. The high-frequency semicircle is assumed to contain contributions from the bulk conductivity of PEO in addition to R_{bulk}. Thus, since the electronic conductivity is more accurately determined by impedance measurements on ion-blocking cells (see Fig. 4i), the authors do not further consider this semicircle.

In principle, symmetrical impedance measurements with electron-blocking contacts can also be realized for oxygen ion conductors. For example, in ref. 48, a CoO bulk sample was sandwiched between two YSZ single crystals, which were covered with Pt paste on the outside. The latter couples the ionic current through the cell and the electronic current through the external circuit *via* the electrochemical oxygen exchange reaction with the surrounding atmosphere. Thus, $Pt|O_2$ provides the reservoir electrode in analogy to Li metal in the previous examples. Although the low-frequency region of the resulting impedance spectra (Fig. 5k) was reconstructed from DC relaxation experiments, it nicely shows the impedance response of a predominant electronic conductor between two electron-blocking contacts, similar to Fig. 5c. Please note, however, that the semicircle observed at medium to high frequencies is attributed to the oxygen exchange impedance of the $Pt|O_2$ electrode rather than the effective bulk resistance. The ionic conductivity of the mixed conductor is thus obtained by fitting the low frequency feature to a W_s element, in series to a high-frequency offset resistance (YSZ bulk resistance) and three $R|Q$ elements to account for all interfaces, assuming $R_{eon} \approx 0$. Although meaningful values of σ_{ion} could be obtained, the various interfacial contributions to the overall impedance highlight the complexity of such measurements and their interpretation.

Measurements with SOFC-type contacting of MIECs

Mixed conducting electrodes in solid oxide fuel or electrolysis cells are always used with asymmetrical contacting, *i.e.* a current collecting electron conductor on one side and an electrolyte on the other side. The resulting circuit model with terminating elements was already discussed above and is shown in Fig. 1g. It is highly illustrative to simulate the impedance response of this transmission line (Fig. 1g) in order to better understand the impact of various terminal resistances and capacitances. However, such a detailed discussion of various possible combinations of

contact selectivities and their effect on the general shape of the impedance spectrum is beyond the scope of this paper; it can be found in ref. 13 (Fig. 7b).

Often, further simplifications are adequate and also required in order to avoid overparameterisation. In a typical simplification, we neglect both charge transfer resistances $R_{ct,i}$ and $R_{ct,e}$ and thus also the terminating impedances Z_A and Z_D. Moreover, $C_{e/i}$ of the coupling impedance $Z_B = Z_{react}$ is often much smaller than C_{chem} and thus also neglected. Finally, we do not take the dielectric capacitance into account (or consider it only in parallel to any additional electrolyte resistance). This leads to the circuit shown in Fig. 6b, which can serve as the starting point for many considerations on quasi-one-dimensional (*e.g.* thin film) SOFC/SOEC electrodes.

The coupling resistance in the ionic rail R_{react} is of very high relevance for MIEC electrodes in SOFC/SOEC applications, since it describes the essential oxygen exchange kinetics of such electrodes. However, this resistance is also the reason that simplifications of the corresponding circuit by employing Warburg elements often fail. Accordingly, such measurements reveal the full potential of the transmission line model, which allows an intuitive description in the form of an equivalent circuit, while still being physically exact in terms of the Nernst–Planck equation eqn (1). In the following, several typical situations are discussed for important SOFC-materials, some of them allowing further simplifications, others requiring additional terminating elements, such as the ionic charge transfer resistance $R_{ct,i} = Z_D$ in the ionic rail. At the end of this section, it is shown that a reaction resistance approaching very high values reflects the transition of a SOFC-type electrode to a battery-type electrode.

Solid oxide fuel and electrolysis cells

Fig. 6a sketches the situation under consideration – a dense SOFC cathode or SOEC anode, with the MIEC being in contact with the oxygen atmosphere and a current collector (O_2|cc) on

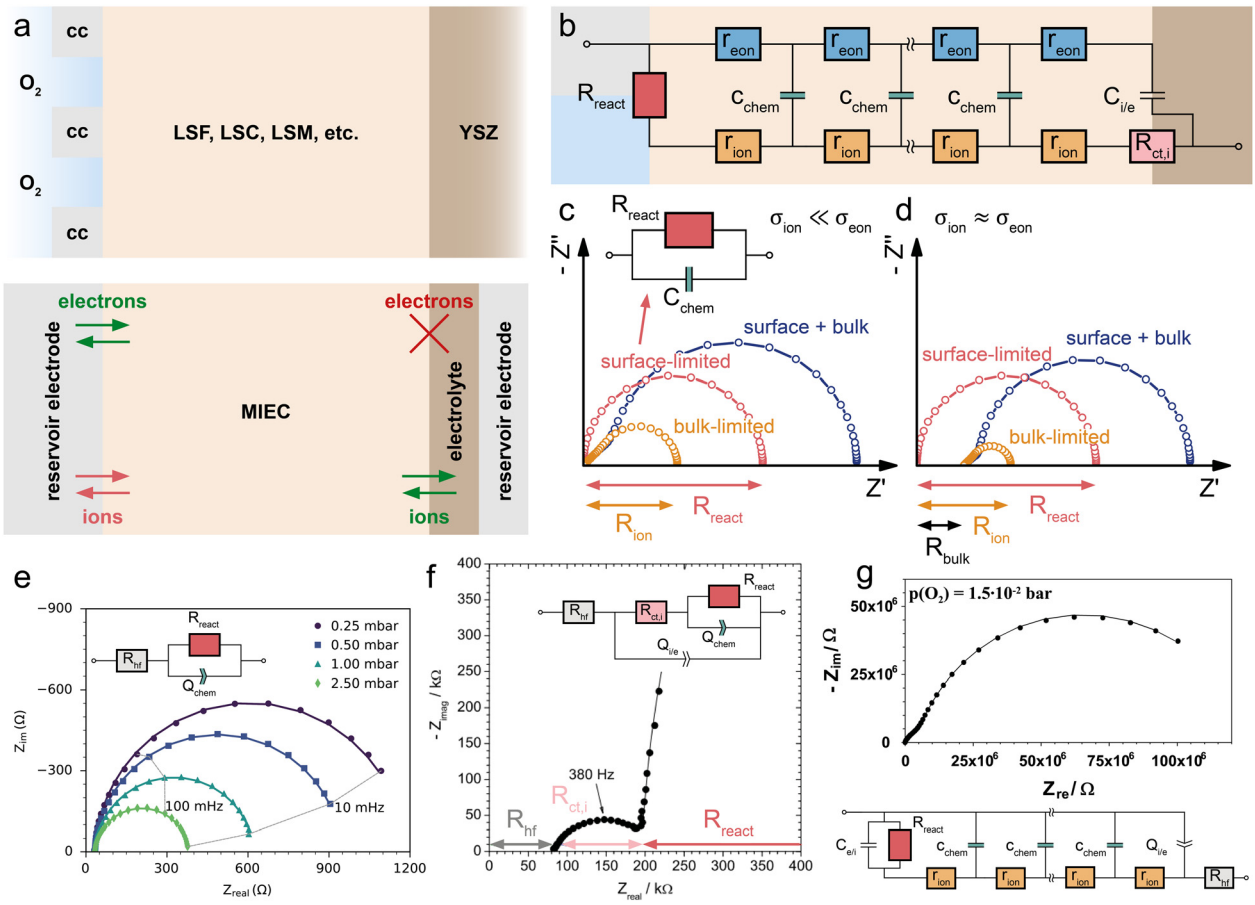

Fig. 6 (a) Sketch (top) and schematic representation (bottom) of a dense SOFC electrode consisting of an MIEC on a YSZ electrolyte, with a current collector (cc) contacting the MIEC on the O_2-exposed side. (b) Adapted transmission line for the SOFC electrode in subfigure (a). (c) Calculated impedance response of the SOFC electrode with a predominant electronic conductor (LSF, $\sigma_{ion} \ll \sigma_{eon}$) for different limiting cases. (d) Calculated impedance response of the SOFC electrode with a mixed conductor (STF at low pO_2, $\sigma_{ion} \approx \sigma_{eon}$) for different limiting cases. (e) p_{O_2}-dependent half-cell impedance spectra of an LSF thin film grown on top of a Pt-grid current collector on a YSZ single crystal. Original image published in ref. 8 under a CC BY license. (f) Impedance response of an LSCF thin film microelectrode on a YSZ single crystal. Image reprinted (adapted) from ref. 49 with permission from Elsevier. (g) Impedance response of an LSM thin film microelectrode on a YSZ single crystal. Image reprinted (adapted) from ref. 50 with permission from John Wiley and Sons. For subfigures (e)–(g), the equivalent circuits used for impedance fits were added to the image.

one side, and the O^{2-} conducting electrolyte (*e.g.* YSZ) on the other side. The MIEC/electrolyte interface presents a fully blocking boundary for electrons, represented by $C_{i/e}$ and may include an ionic charge transfer resistance $R_{ct,i}$ in the ionic rail. It is obvious from Fig. 6b that the impedance of the simplified equivalent circuit is limited by either surface exchange (R_{react}) or bulk transport (R_{ion}, R_{eon}) (or ionic charge transfer $R_{ct,i}$, if relevant).

In the case of a predominant electronic conductor such as LSF, LSM or LSC, the resistances on the electronic rail can be neglected ($R_{eon} = 0$), and the electrode's impedance response often falls into one of three categories, as shown in Fig. 6d. If the surface exchange resistance dominates and bulk transport resistances can be neglected ($R_{ion} = 0$), a simple $R_{react}|C_{chem}$ semicircle results, which is observed, for example, for many SOFC thin film electrodes at high operating temperatures.[40,41,49,51,52] Fig. 6e exemplarily shows a set of p_{O_2}-dependent impedance measurements on an LSF thin film electrode, taken from ref. 8, which consist of a high-frequency offset due to the YSZ electrolyte resistance followed by a mid- to low-frequency $R_{react}|Q_{chem}$ semicircle.

In many studies on such or similar thin film electrodes, however, an additional mid-frequency arc was observed, and in ref. 53 this was shown to be due to the ion transfer resistance at the MIEC/electrolyte interface $R_{ct,i}$. Still neglecting all transport resistances ($R_{ion} = R_{eon} = 0$) leads to the equivalent circuit in Fig. 6f, which excellently fits the measured impedance spectra of many MIEC thin film electrodes on YSZ (with constant phase elements replacing the capacitors).

Next, we discuss the interplay of R_{ion} and R_{react} in the representative circuit Fig. 6b. In the case that the bulk transport resistance R_{ion} is much higher than the surface exchange resistance (bulk-limited electrode), R_{react} can be neglected and replaced by a short circuit. In the limit of negligible R_{eon} and $C_{i/e}$, the resulting impedance response corresponds to a finite-length Warburg element (Fig. 2b). The crucial difference between the traditional W_s element and a bulk-limited SOFC electrode becomes visible once R_{react} can no longer be neglected. While the traditional W_s element would imply a simple serial $W_s + R_{react}$ connection with a corresponding real-axis offset in the Nyquist plot, the physically more accurate transmission line in Fig. 6b predicts a merging of the surface resistance into the bulk transport feature, as shown in Fig. 6c (surface + bulk) by the emerging semicircle. In reality, the surface exchange resistance R_{react} is rarely negligible compared to bulk transport resistances, at least not for $C_{chem} \gg C_{e/i}$. Literature examples of dense SOFC or SOEC electrodes exhibiting only a simple Warburg impedance response are therefore hard to find.

An experimental example of a mixed surface-bulk-limited SOFC electrode can be found in ref. 50, where the partial pressure dependence and rate limiting steps of the oxygen reduction kinetics on LSM thin films is examined. The impedance response (Fig. 6g) consists of a low-frequency semicircle with a mid-frequency shoulder, which is ascribed to an ionic transport limitation across the LSM thin film at high oxygen partial pressures (*i.e.* low oxygen vacancy concentrations). The measured spectra were fitted using the transmission line shown in Fig. 6g, which is equivalent to the circuit in Fig. 6b for $R_{ct,i} = R_{eon} = 0$ with an additional high-frequency offset resistance R_{hf} and an interfacial capacitance $C_{e/i}$ in parallel to the surface exchange resistance. The resulting fit allowed a separate analysis of the bulk transport and oxygen exchange kinetics in LSM.

For balanced mixed conductors with similar σ_{ion} and σ_{eon}, such as STF at low pO_2,[43] the consideration of electronic bulk resistances requires the full transmission line (Fig. 6b). As shown in the simulated spectra of Fig. 6d, the impedance response is shifted by a real axis offset corresponding to R_{bulk} (eqn (26)) if the electronic bulk transport resistance cannot be neglected. Only in the surface-limited case, the impedance response is equivalent to that of a predominant electronic conductor, as it transforms into a simple $R_{react}|C_{chem}$ semicircle. Please note that the above discussion only considers the impedance response of the isolated MIEC sample and its interfaces. In reality, impedance spectra from two-electrode measurements usually contain additional contributions from, for example, the electrolyte and the counter electrode.[41] However, these contributions can simply be considered in series to the MIEC impedance. Especially the electrolyte resistance is often well separated in the Nyquist plot, due to different time constants of the corresponding transport processes. Thus, their inclusion in the equivalent circuit is straightforward.

From SOFC to battery electrodes

A highly interesting transition occurs when the oxygen exchange reaction at an SOFC electrode surface is more and more blocked, as shown in Fig. 7. Starting from a bulk-limited electrode ($R_{react} = 0$) of a predominant electronic conductor ($R_{eon} = 0$), such as LSF, the impedance spectrum initially corresponds to that of a finite-length Warburg element (W_s) characterized by R_{ion} and C_{chem} (Fig. 7b, *cf.* also Fig. 6c). When the oxygen surface exchange with the surrounding atmosphere is more and more blocked, R_{react} increases. This can be achieved, for example, by covering the current collector and MIEC with a dense capping layer of negligible ionic conductivity. As a consequence, the impedance response first transitions away from the simple W_s element into a mixed regime, where both R_{react} and R_{ion} are relevant. For further increasing oxygen exchange resistances, the high frequency 45° part of the spectrum remains nearly unchanged, but the low frequency end transforms into a more and more separate semicircle dominated by the growing R_{react}. If the capping layer is perfectly blocking ($R_{react} \to \infty$), the semicircle becomes infinitely large, such that it effectively transforms into a capacitor with a capacitance C_{chem}. For the transmission line in Fig. 6b, this implies that the connection between the left contact and the ionic rail of the MIEC can be considered as fully disrupted. Thus, the resulting circuit is equivalent to the transmission line representation of a finite-space Warburg element (W_o, Fig. 2c). However, for small C_{chem}, a coupling capacitor $C_{e/i}$ might come into play at the current collector/MIEC interface.

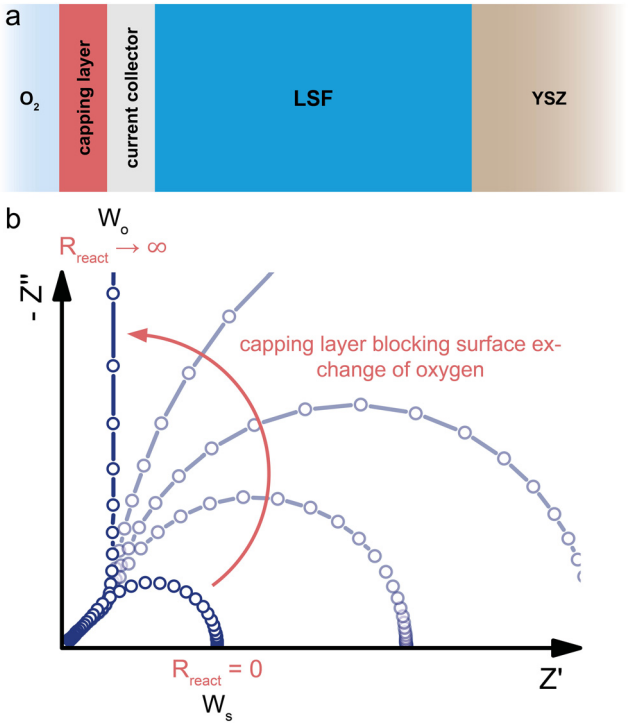

Fig. 7 (a) Schematic sketch of a dense SOFC electrode consisting of a predominant electronic conductor (LSF, $\sigma_{ion} \ll \sigma_{eon}$) on a YSZ electrolyte contacted by a current collector on the O_2-exposed side. A capping layer blocks the surface exchange reaction between the O_2 atmosphere and the LSF surface. (b) Evolution of the calculated impedance response (circuit Fig. 6b with $R_{eon} = 0$) for an increasing surface exchange resistance R_{react} due to the capping layer, showing the gradual transition from a W_s to a W_o type behavior.

In terms of equivalent circuits, blocking the surface exchange reaction of an SOFC electrode corresponds to a transition from (quasi) finite-length (W_s) to finite-space (W_o) diffusion, with the intermediate region lying beyond the applicability of classical two-terminal Warburg elements. This emphasizes once more the consistency of the general transmission line model with the specific solutions to Fick's first law of diffusion for the respective boundary conditions, and shows that the separate consideration of ionic and electronic transport across the contact interfaces is required to accurately describe realistic measurement setups of SOFC electrodes with a finite, nonzero R_{react}. In terms of device functionality, this transition constitutes the transformation of an SOFC electrode into an oxygen-ion battery electrode, which can store charge based on the principle of coulometric titration.[17,54]

Measurements with battery-type contacting of MIECs

When an MIEC is contacted by an ideal ionic conductor on one side and by an ideal electronic conductor on the other, neither ions nor electrons can be transferred across both interfaces, leading to a purely capacitive behaviour for $\omega \to 0$. This is the typical situation found for battery electrodes and the simplest case of such a measurement was already discussed above as the limiting case in the transition of a (simplified) SOFC electrode to a battery electrode. In such a situation, the only way a direct current through the external circuit can be charge-balanced is by filling or emptying the chemical capacitance of the material, depending on the current direction.

For a more detailed discussion of insertion electrodes, we start with the battery-type model circuit in Fig. 1f, i.*e.* we consider a mixed conducting LIB cathode material LiM_xO_y contacted by an electronic conductor (current collector) on one side and an ionic conductor (electrolyte) on the other. A reasonable simplification of the transition line model for such electrodes is shown in Fig. 8a. We assume an ideal electronic contact of the current collector to the MIEC and thus $R_A = R_{ct,e} = 0$. Electrochemical reactions of ions at the current collector are completely neglected ($R_B \to \infty$), and also the interfacial capacitance $C_B = C_{e,i}$ is neglected, assuming it is much smaller than C_{chem}. At the MIEC electrolyte interface, electrons are often assumed to be completely blocked by the absence of any electrochemical reaction ($R_C = R_{react} \to \infty$). Then, only an interfacial capacitor $C_{i,e}$ couples the electronic to the ionic rail. Here, however, the consequences of side reactions are also discussed and thus we keep the resistor $R_C = R_{react}$ in the circuit, here denoted R_{sr} (sr = side reaction). Ions, on the other hand, can move into the electrolyte with a charge transfer resistance $R_{ct,i}$.

Bulk transport and side reactions

In a first step, we discuss the influence of bulk transport resistances and electrochemical side reactions with the electrolyte on a battery electrode's impedance response. For this purpose, we set the charge-transfer resistance $R_{ct,i}$ and the double layer capacitance $C_{i,e}$ to zero and consider only changes in R_{eon} and R_{sr}. Under common operating conditions, LIB cathode materials are usually predominant electronic conductors with $\sigma_{ion} \ll \sigma_{eon}$, and the assumption of negligible electronic bulk resistance ($R_{eon} = 0$) is therefore justified in most cases. If the electron transfer between MIEC and electrolyte is perfectly blocked (*i.e.* no electrochemical side reactions such as electrolyte oxidation or reactions with impurities, $R_{sr} \to \infty$) the resulting transmission line corresponds to that of a finite-space Warburg element (W_o, Fig. 2c). The Nyquist plot of W_o features a high-frequency semi-infinite (45°) and a low-frequency capacitive (90°) regime, with $R_{ion}/3$ being the real part and $-1/\omega C_{chem}$ the imaginary part of the impedance in the low-frequency limit, as shown in Fig. 8b. This exactly corresponds to the limiting impedance of the capped SOFC electrode in Fig. 7 with $R_{react} \to \infty$.

In reality, battery electrodes exhibit a finite R_{sr}, and the validity of the assumption $R_{sr} \to \infty$ often merely depends on the low-frequency limit of the measurement. As demonstrated in Fig. 8b, a decrease of R_{sr} causes the capacitive low-frequency end of the spectrum to bend downwards into a semicircle that reaches the real axis for $\omega \to 0$. In practice, properly assembled battery cells still exhibit a very high R_{sr}, such that only a minor bending can be observed within common frequency ranges.[5]

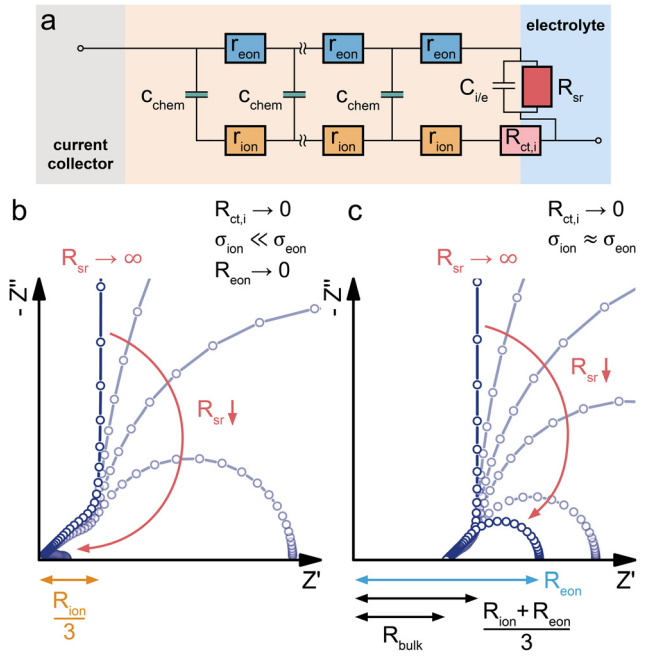

Fig. 8 (a) Schematic sketch of a dense Li insertion electrode consisting of an MIEC of the general composition LiM_xO_y between an ideal (ion-blocking) current collector and an electrolyte. (b) Adapted transmission line for a battery-type setup of an MIEC sandwiched between an ion-blocking current collector and an electron-blocking electrolyte. A finite resistance R_{sr} is considered between the MIEC electronic rail and the electrolyte to account for possible side reactions with the electrolyte. (b) Impact of a decreasing R_{sr} on the calculated impedance response of a battery electrode for a predominant electronic conductor ($\sigma_{ion} \ll \sigma_{eon}$) with a negligible charge-transfer resistance $R_{ct,i}$. (c) Impact of a decreasing R_{sr} on the calculated impedance response of a battery electrode for a mixed conductor ($\sigma_{ion} \approx \sigma_{eon}$) with a negligible charge-transfer resistance $R_{ct,i}$.

For a finite R_{eon}, the transmission line moves beyond the assumptions and applicability of the classical W_o element and transforms into a more general ambipolar diffusion element with reflective boundary conditions. The corresponding impedance response is shown in Fig. 8c. For $R_{sr} \to \infty$, it is closely related to that of W_o, with a real axis offset R_{bulk} (eqn (26)) and a low-frequency limiting real part $(R_{ion} + R_{eon})/3$. Please note that the transition from Fig. 8b to c is fully analogous to the transition from Fig. 5c to e. In both cases, the transmission line allows a straightforward generalisation of the Warburg elements to include the presence of electrical potential gradients (*i.e.* nonzero electronic resistance). In practice, the bulk transport in battery or solid oxide cell electrodes is most often limited by ion conduction, and electronic resistances rarely need to be considered. Even in phosphate-based Li insertion materials such as $LiFePO_4$ (LFP), where the isolating PO_4^{3-} groups lead to an intrinsically poor electronic conductivity, ionic conductivities are still significantly lower,[47,55] and no substantial high-frequency offset is observed in impedance spectra.[56–59] Also for NVPF Na-insertion electrodes ($\sigma_{ion} \gg \sigma_{eon}$ near the stoichiometric composition), SOC-dependent impedance measurements do not show a significant variation of the high-frequency offset, despite severe diffusion limitations (45° Warburg feature) at low frequencies.[60] This suggests that NVPF transitions into a predominant electronic conductor upon charging, already at low SOC, such that $R_{eon} = 0$ can again be assumed.

Charge transfer and the validity of Randles' circuit

Having established the impact of bulk transport resistances and side reactions on the impedance spectrum, we now consider some special cases and simplifications of the impedance model of dense Li insertion electrodes. For the sake of completeness, we also add a high-frequency offset resistance R_{hf} in series to the transmission line to account for the sum of ohmic contributions from the electrolyte and other cell components.

If R_{eon} can be neglected ($R_{eon} = 0$), as in the case of a predominant electronic conductor with $\sigma_{ion} \ll \sigma_{eon}$, the electronic rail can be replaced by a short circuit. The remaining part of the transmission line (Fig. 9a) then corresponds to a serial connection of a W_o element (*cf.* Fig. 2c) and $R_{ct,i}$ in parallel to the $R_{sr}|C_{i/e}$ element, with R_{hf} still in series to everything else. The resulting simplified equivalent circuit (Fig. 9b) differs from the original Randles' circuit (Fig. 9c) merely by the presence of a finite side-reaction resistance R_{sr} in parallel to $C_{i/e}$. Thus, for $R_{eon} = 0$ and $R_{sr} \to \infty$, the transmission line in Fig. 9a is identical to Randles' circuit and provides a physical justification for the connectivity of its constituent elements. Please note that such a simplification is only valid for $R_{eon} = 0$, and that otherwise the full transmission line (Fig. 8a) has to be applied.

In particular, the consistency of the transmission line with Randles' circuit requires placing $C_{i,e}$ on the electronic rather than the ionic rail terminal. If a capacitor was placed on the ionic rail ($C_{i,i}$), it would end up in parallel to $R_{ct,i}$ (but in series to W_o) in the simplified circuits Fig. 9b and c. Furthermore, these considerations show that a finite R_{sr} can be accounted for by simply adding it in parallel to $C_{i,e}$ in Randles' circuit, without needing to use the full transmission line for impedance fits. Such a circuit was successfully applied to Li insertion electrodes, for example, in ref. 5, where the impedance of epitaxial LMO thin films on $SrRuO_3$ (SRO) was analysed. In this case, the W_o element was substituted by an anomalous diffusion element W_o^* to account for a non-ideal behaviour of the LMO thin film electrode (see ref. 5 for details). The corresponding impedance spectra and the equivalent circuit used for fitting are shown in Fig. 9e–g. It is worth noting that the relevance of R_{sr} for the impedance fit depends on the relative magnitudes of $C_{i/e}$ and C_{chem}. While the low-frequency onset of a large semicircle is clearly visible and excellently captured by the fit in Fig. 9e (3.82 V *versus* Li, low C_{chem}), R_{sr} becomes effectively infinite for the purpose of fitting in Fig. 9f (4.20 V *versus* Li, high C_{chem}), as the chemical capacitance dominates the nearly vertical low-frequency response.

Final remarks on more complex materials and systems

All these examples demonstrate that already for simplified materials, systems and geometries a broad range of spectra

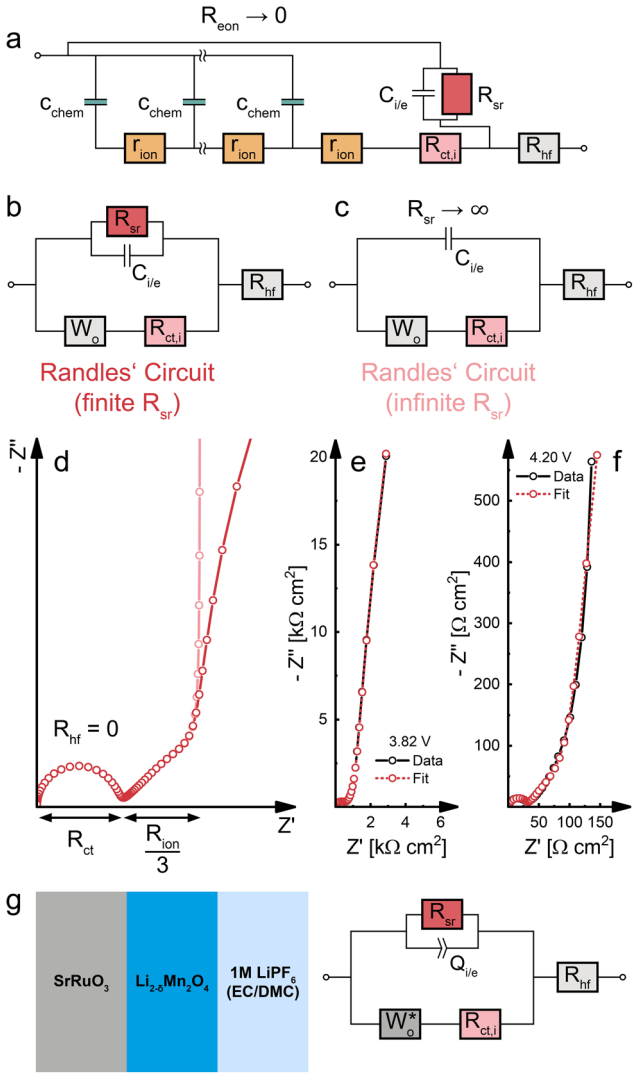

Fig. 9 (a) Simplified transmission line for a dense Li insertion electrode with $\sigma_{ion} \ll \sigma_{eon}$ ($R_{eon} \approx 0$). The electronic rail is replaced by a short circuit, allowing the replacement of the transmission line by a W_o element. A high-frequency offset resistance R_{hf} has been added in series to account for ohmic impedance contributions from the electrolyte and other cell components. (b) Randles' circuit with a finite R_{sr} in parallel to $C_{i/e}$. (c) Classical Randles' circuit, assuming an infinite R_{sr}. (d) Calculated impedance responses of the circuits from subfigures (b) and (c), where R_{hf} has been neglected in both cases. (e) Half-cell impedance spectra of an LMO thin film electrode at 3.82 V *versus* Li (low C_{chem}). Diagram reproduced with data from ref. 5. (f) Half-cell impedance spectra of an LMO thin film electrode at 4.20 V *versus* Li (high C_{chem}). Diagram reproduced with data from ref. 5. (g) Sample sketch and equivalent circuit used for fitting the impedance spectra (e) and (f).

shapes may result. Situations often further complicate for "real world" samples or electrochemical cells. Not surprisingly there is no general recipe how to treat such "real systems" but some final comments shall illustrate, how additional features may be considered.

Imperfect contacts and secondary phases

As a first group of non-idealities we discuss two modifications of the ionic or electronic contacts: mechanically imperfect contacts (*e.g.* large pores along interfaces) and additional chemical phases at interfaces, such as SEIs (solid electrolyte interphases) in lithium (ion) batteries.

Severe lateral inhomogeneities may easily occur at solid/solid interfacial contacts which rely on a pressure applied to keep the solids together. Examples are MIECs or solid electrolytes in contact with a metal plate (*e.g.* Li-plate on a ceramic Li conductor,[61] Ag-plate on CaF_2,[62] *etc.*). In such cases, gaps or pores between the two solids exist in parallel to regions with tight (atomistic) contact. The contacted areas may still behave like the terminals discussed so far, *i.e.* they might be treated by $R|C$ elements. The gaps, on the other hand, exhibit virtually infinite DC resistances and can be described locally by a geometrical capacitor with a certain gap thickness and a gap permittivity. Such a "bad contact" leads to a frequency-dependent three-dimensional current distribution and in general one-dimensional equivalent circuits are inadequate to map this situation.

However, as shown by finite element simulations, such imperfect contacts on solid electrolytes often lead to an additional (though not perfectly ideal) semicircle in the complex impedance plane.[62,63] The resistance of this additional arc is strongly related to the current constriction in the solid electrolyte, which is unavoidable in the DC case in order to pass the contact bottleneck. The capacitance, on the other hand, can often be approximated by the geometrical gap capacitor. A fit of such spectra to two serial $R|C$ elements allows an approximative interpretation: the high frequency elements represent the bulk conductivity and permittivity values as if a perfect contact was used. More details of such effects for specific geometrical situations of contacted solid electrolytes can be found in ref. 61–64, and a detailed discussion of its relevance for solid-state lithium batteries is given in ref. 61.

Very similar current constriction phenomena are expected for MIECs with geometrically imperfect contacts and thus also additional impedance features can be expected. However, those are possibly more complicated in shape (compared to simple semicircles), since the sample parts with constricted current lines, *i.e.* close to the contact points, also behave as transmission lines. Their expected relaxation frequencies strongly depend on the geometrical situation (contact size and distance, gap thickness) and the corresponding impedance features might easily overlap with other features of the terminal elements. The relaxation frequency dependence on the local contact geometry (and thus, for example, on pressure) may help identifying "bad contact features" of MIECs.

Secondary interfacial phases are another cause of severe deviations from our simple model of charge transfer and reaction impedances at ionic and electronic contacts. Examples are SEIs in lithium (ion) batteries or interfacial reaction zones between perovskite-type MIEC electrodes and zirconia electrolytes in SOFCs. Even if such a secondary phase is a homogeneous pure ion conductor (with low ionic conductivity) it leads to substantial changes of the terminal impedances. We discuss this for the ionic contact of an MIEC at the example of an SEI. The charge transfer resistance already present in the transmission

line now represents the charge transfer from the MIEC into the SEI $\left(R'_{ct,i}\right)$. This is followed by an SEI bulk resistance R_{SEI} and a second charge transfer resistance from the SEI into the electrolyte $\left(R''_{ct,i}\right)$. The resulting circuit is shown in Fig. 10a. Please note that the electronic coupling capacitor $C_{i/e}$ enters the ionic rail in front of the SEI bulk resistance. As a consequence, it is no longer possible to use the analytical solution of our transmission line model with four terminals. Supposed both charge transfer resistances are small compared to the ionic bulk resistance of the SEI R_{SEI} we end up with the simple circuit shown in Fig. 10b: the bulk-type $R|C$ element of the SEI is simply in series to a Warburg impedance in parallel to $C_{i/e}$. This means that the bulk of an SEI layer should be considered by a separate serial element rather than by combining it with the charge transfer resistance in a Randles circuit.

Real SEI layers are chemically and geometrically complex and may consist of several phases.[65,66] This causes a distribution of relaxation times, which might empirically be considered by using a constant phase element instead of the bulk capacitor $C_{SEI,diel}$.[67] In general, such constant phase elements are often more adequate than capacitors for describing interfacial capacitances and may thus be used at all terminals instead of ideal capacitors. However, the physical reasons causing such "non-ideal capacitors" are often unknown. The situation becomes even more complex when the secondary phase itself is also a mixed conductor. Then two transmission lines have to be combined in series, with both resistive rails transmitting into the second phase, possibly bridged by two charge transfer impedances, see Fig. 10c. Most importantly, it is not possible to simply add the two individual transmission line impedances, and thus also analytical solutions are usually no longer possible.

Porous electrodes

The second group of non-idealities frequently met in solid oxide cells and batteries are porous electrodes. Interestingly, extensions of the one-dimensional transmission line model for these two types of porous electrodes are rather different.

In solid oxide cells, porous MIEC gas diffusion electrodes are quite common on the oxygen side, the pores being filled

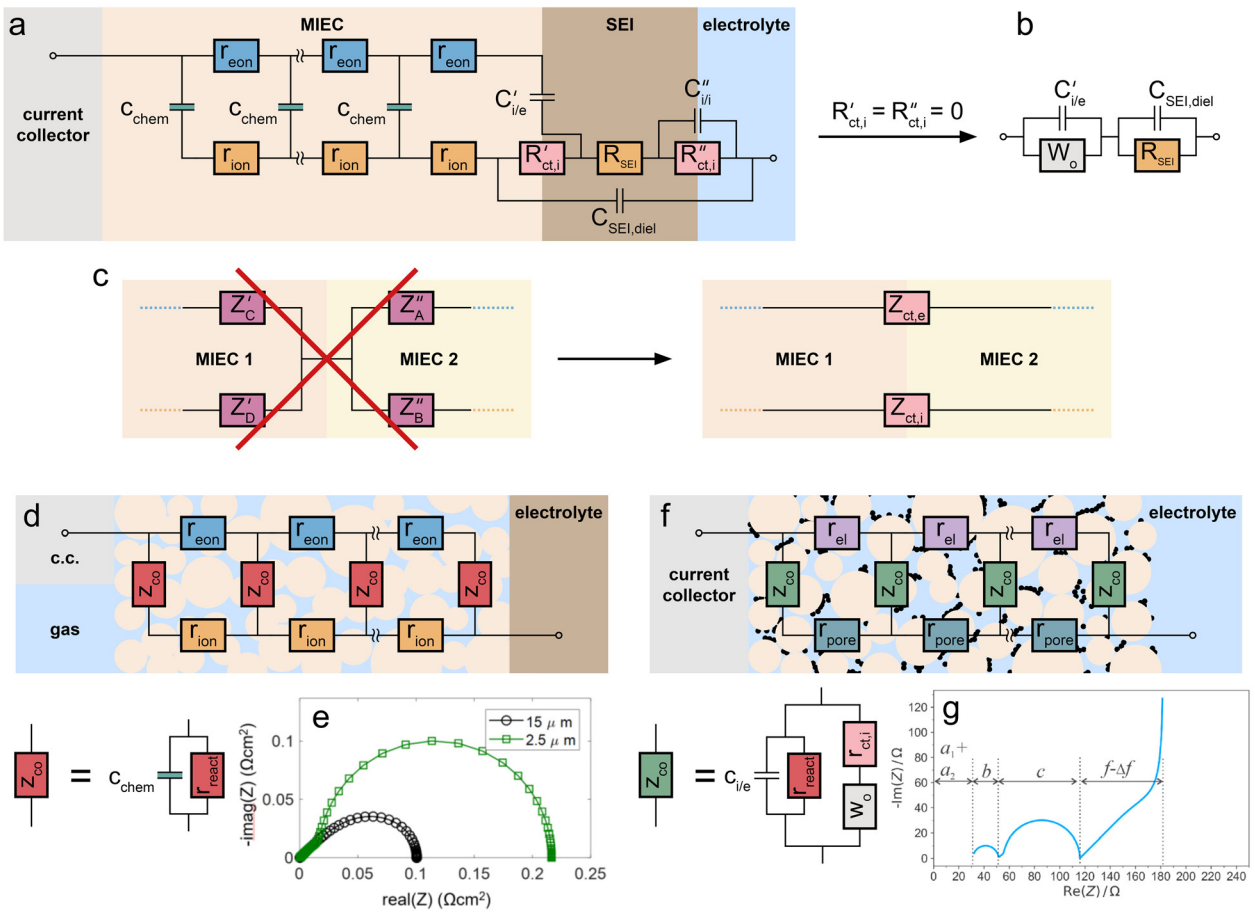

Fig. 10 (a)–(d) Schematic transmission line for a porous solid oxide electrode. The element c_{chem} is replaced by a general differential coupling impedance z_{co}, which in this case corresponds to a simple $r_{react}|c_{chem}$ element. For simplicity, charge transfer resistances are neglected. (e) Simulated impedance spectra for porous SOFC electrodes of 2.5 μm and 15 μm thickness. Original image published in ref. 4 under a CC-BY 4.0 license. (f) Schematic transmission line for a porous battery electrode. For negligible r_{eon}, the coupling impedance z_{co} corresponds to a Randles circuit, here with a finite side reaction resistance r_{react} (g) Simulated impedance spectrum for a de-Levie-type battery transmission line, similar to the circuit in (f). Reprinted with permission from ref. 2.

with the gaseous phase, thus enabling the coupling oxygen exchange reaction along the entire MIEC material. The complex tortuous conduction pathways along the thickness coordinate (distance from the electrolyte) are modelled by dividing the ionic/electronic conductivities by a microstructural factor M, given by $\sigma_{\mathrm{eff}} = \sigma_{\mathrm{bulk}}/M$. Additionally, the coupling between ionic and electronic current can be much more complex than the mere chemical capacitance, since coupling fluxes between the two rails are also possible *via* the oxygen exchange reaction at the surface. Therefore, instead of differential c_{chem} elements, differential coupling elements z_{co} are used, see Fig. 10d. Such a circuit is often called a de Levie model.[68] The coupling impedances z_{co} can often be approximated by $r_{\mathrm{react}}|c_{\mathrm{chem}}$ elements, with r_{react} corresponding to the oxygen exchange reaction at the MIEC surface (*cf.* Fig. 6c). For the rather common case of sufficiently thick and good electron conducting electrodes, this results in a Gerischer-type impedance[69] shown by the black spectrum in Fig. 10e, given by the equation

$$Z_{\mathrm{g}} = \frac{R_{\mathrm{dc}}}{\sqrt{1 + i\omega\tau}}, \tag{27}$$

where $R_{\mathrm{dc}} = \sqrt{R_{\mathrm{ion}} R_{\mathrm{react}}}$ and $\tau = R_{\mathrm{react}} C_{\mathrm{chem}}$. Finite electrode thickness, interfacial resistances[4] and gas diffusion limitations[70,71] make impedance models of real-world electrodes even more complex.

In batteries based on liquid electrolytes, on the other hand, porous electrodes are filled with electrolyte, leading to a strongly enhanced area of the electrode/electrolyte interface. Furthermore, carbon black is commonly added to the porous electrode to minimise the electronic contact resistance between the active material (MIEC) particles, as shown in Fig. 10f. Thus, the conduction pathways and overpotentials are more complex and consideration of ion transport in the electrolyte (in pores) causes an additional transmission line, with r_{el} representing the incremental effective electronic resistance of the electrode and r_{pore} being the incremental resistance of ion transport through the electrolyte-filled pores, both along the thickness coordinate. In this case, the coupling impedance z_{co} describes the coupling of electronic charge carriers in the MIEC to ions in the electrolyte. This coupling includes interfacial charge transfer and ambipolar diffusion through the MIEC particles. For the typical case that the MIEC is predominantly electron conducting, z_{co} takes the form of a Randles circuit (Fig. 10f).[2] Since the W_{o} element corresponds to a simplified transmission line itself (Fig. 2c), the circuit shown in Fig. 10f can be considered as the MIEC's bulk transmission line nested into the structural transmission line of the porous electrode. In the corresponding impedance spectrum (Fig. 10g), arc *b* is due to the MIEC/current collector impedance, which is neglected in the circuit displayed here. Arc *c* is a convoluted feature with contributions primarily from r_{pore} (electrolyte conduction in pores) and $r_{\mathrm{ct}}|c_{\mathrm{i/e}}$ elements, whereas the feature *f* is the Warburg impedance in Randles' circuit that models the ambipolar Li diffusion within the particles. Again, real world electrodes are even more complex due to mobility of the PF_6^- anions, which causes concentration polarisation in the liquid electrolyte,[2] SEI formation, or non-uniform distributions of particle shapes and sizes.

Multiple charge carriers

Materials that have more than two charge carriers can still be described by an extended transmission-line model with one rail for each carrier and coupling by chemical capacitors for each species.[72] Typical examples here are proton conducting oxides that contain protons, oxygen vacancies and electrons as mobile species,[73] as well as multi-ion liquid electrolytes.[72] The treatment of such materials becomes tremendously more complex, because multiple ambipolar diffusion coefficients come into play. In solid proton conductors, for example, the H_2O molecule, the H atom and the O atom can all diffuse as neutral species, each with a different diffusion coefficient. Additionally, boundary conditions for each carrier must be specified. The impedance of such circuits requires numerical computation.

Conclusions

The impedance of dense mixed ionic and electronic conductors (MIECs) is consistently described by a one-dimensional transmission line consisting of two resistive rails for ion and electron conduction, coupled by chemical capacitors. The resulting circuit is physically exact in terms of the Nernst–Planck equation and provides a highly intuitive and practical approach to understanding and evaluating the impedance responses of various MIEC devices. Four terminal $R|C$ elements at the rail ends allow a tailored adaptation of the general transmission line to specific measurement configurations, which can be classified as symmetrical (*e.g.* setups for the characterisation of bulk properties), SOFC-type and battery-type. For deciding which terminal elements should be used and which one may be negligible, it is helpful to distinguish between two types of terminals: those where the corresponding charge carrier can simply pass to the contact by charge transfer and those where an electrochemical reaction is required to couple a blocked resistance rail to the still transmissive rail.

Besides providing a universal starting point for the intuitive derivation of tailored, physically exact impedance models, the general transmission line provides several key insights:

(1) Equivalent circuit elements can either represent charge transport resistances or the rates of electrochemical reactions that couple electron and ion currents. This difference becomes graphically clear in a transmission line picture.

(2) The general transmission line is consistent with the classical finite Warburg elements W_{s} and W_{o}, which are derived from Fick's law of diffusion for negligible electrical potential gradients ($\sigma_{\mathrm{ion}} \ll \sigma_{\mathrm{eon}}$) under the corresponding boundary conditions.

(3) The resistive and capacitive circuit elements in the corresponding transmission lines of the Warburg elements can be identified as the incremental ionic resistance r_{ion} ($R_{\mathrm{ion}} = \sum r_{\mathrm{ion}}$) and the incremental chemical capacitance c_{chem} ($C_{\mathrm{chem}} = \sum c_{\mathrm{chem}}$), respectively.

(4) The general transmission line provides an extension of these Warburg elements for MIECs with finite σ_{eon} (*e.g.* $\sigma_{ion} \approx \sigma_{eon}$) by considering a resistive rail for electronic transport with $R_{eon} = \sum r_{eon}$.

(5) For measurements with symmetrical contacts that are completely blocking towards one charge carrier and fully transmissive towards the other, the impedance spectrum consists of two arcs, with a shape and size reflecting the relevance of ionic and electronic contributions.

(6) For an additional charge transfer resistance, the spectrum consists of three arcs, all of which can be fitted to a single transmission line circuit.

(7) The impedance response of a bulk-limited SOFC electrode with negligible surface resistances corresponds to a finite-length Warburg element (W_s), due to the symmetry of the W_s transmission line. For a non-negligible surface exchange resistance, neither W_s nor a serial connection of W_s and the surface exchange resistance appropriately describe the electrode impedance. Only the full transmission line allows a physically meaningful interpretation of the corresponding impedance spectra.

(8) An SOFC electrode can be transformed into an oxygen-ion battery electrode by blocking the oxygen exchange reaction at the MIEC surface.

(9) Randles' circuit is a special case of the general asymmetric transmission line model, where $\sigma_{ion} \ll \sigma_{eon}$, and only one interfacial capacitance $C_{i/e}$ at the MIEC|electrolyte interface. Thus, for the given boundary conditions, Randles' circuit can be considered as physically exact in terms of the Nernst–Planck equation.

(10) Within Randles' circuit, a finite side-reaction resistance R_{sr} can be placed in parallel to $C_{i/e}$ to consider, for example, electrolyte oxidation or reactions with impurities in the electrolyte, while remaining fully consistent with the general transmission line.

(11) A finite electronic resistance hinders the application of a simple Randles' circuit and causes a serial high-frequency offset $R_{bulk} = (R_{ion}^{-1} + R_{eon}^{-1})^{-1}$ in the impedance spectrum.

Author contributions

A. E. Bumberger: conceptualisation (equal), investigation, writing – original draft, A. Nenning: writing – review & editing, J. Fleig: supervision, conceptualisation (equal), writing – review & editing.

Conflicts of interest

There are no conflicts to declare.

Acknowledgements

The authors acknowledge TU Wien Bibliothek for financial support through its Open Access Funding Program.

References

1 A. Flura, C. Nicollet, S. Fourcade, V. Vibhu, A. Rougier, J. M. Bassat and J. C. Grenier, *Electrochim. Acta*, 2015, **174**, 1030–1040.
2 J. Moskon and M. Gaberscek, *J. Power Sources Adv.*, 2021, **7**, 100047.
3 J. Moskon, J. Zuntar, S. D. Talian, R. Dominko and M. Gaberscek, *J. Electrochem. Soc.*, 2020, **167**, 140539.
4 A. Nenning, C. Bischof, J. Fleig, M. Bram and A. K. Opitz, *Energies*, 2020, **13**, 987.
5 A. E. Bumberger, C. Boehme, J. S. Ring, S. Raznjevic, Z. Zhang, M. Kubicek and J. Fleig, *Chem. Mater.*, 2023, **35**, 5135–5149.
6 A. E. Bumberger, S. Raznjevic, Z. L. Zhang, G. Friedbacher and J. Fleig, *J. Mater. Chem. A*, 2023, **11**, 24072–24088.
7 A. E. Bumberger, C. Steinbach, J. Ring and J. Fleig, *Chem. Mater.*, 2022, **34**, 10548–10560.
8 A. Schmid, G. M. Rupp and J. Fleig, *Phys. Chem. Chem. Phys.*, 2018, **20**, 12016–12026.
9 W. Lai and S. M. Haile, *J. Am. Ceram. Soc.*, 2005, **88**, 2979–2997.
10 H. Rickert, *Electrochemistry of Solids*, Springer, Berlin, Heidelberg, 1st edn, 1982.
11 C. Ho, I. D. Raistrick and R. A. Huggins, *J. Electrochem. Soc.*, 1980, **127**, 343–350.
12 J. R. Macdonald, *J. Chem. Phys.*, 1973, **58**, 4982–5001.
13 J. Jamnik and J. Maier, *J. Electrochem. Soc.*, 1999, **146**, 4183–4188.
14 J. Jamnik and J. Maier, *Phys. Chem. Chem. Phys.*, 2001, **3**, 1668–1678.
15 J. Jamnik, J. Maier and S. Pejovnik, *Electrochim. Acta*, 1999, **44**, 4139–4145.
16 M. Adamic, S. D. Talian, A. R. Sinigoj, I. Humar, J. Moskon and M. Gaberscek, *J. Electrochem. Soc.*, 2019, **166**, A5045–A5053.
17 A. Schmid, M. Krammer and J. Fleig, *Adv. Energy Mater.*, 2023, **13**, 2203789.
18 J. Maier, *Z. Naturforsch. B*, 2020, **75**, 15–22.
19 V. F. Lvovich, *Impedance Spectroscopy Applications to Electrochemical and Dielectric Phenomena*, John Wiley & Sons, Ltd, New Jersey, 2012.
20 M. Gerstl, G. Friedbacher, F. Kubel, H. Hutter and J. Fleig, *Phys. Chem. Chem. Phys.*, 2013, **15**, 1097–1107.
21 J. Jiang, W. Shen and J. L. Hertz, *Solid State Ionics*, 2013, **249**, 139–143.
22 I. Kosacki, C. M. Rouleau, P. F. Becher, J. Bentley and D. H. Lowndes, *Solid State Ionics*, 2005, **176**, 1319–1326.
23 C. Peters, A. Weber, B. Butz, D. Gerthsen and E. Ivers-Tiffee, *J. Am. Ceram. Soc.*, 2009, **92**, 2017–2024.
24 Y. Hamon, A. Douard, F. Sabary, C. Marcel, P. Vinatier, B. Pecquenard and A. Levasseur, *Solid State Ionics*, 2006, **177**, 257–261.
25 E. Navickas, M. Gerstl, G. Friedbacher, F. Kubel and J. Fleig, *Solid State Ionics*, 2012, **211**, 58–64.
26 C. Ahamer, A. K. Opitz, G. M. Rupp and J. Fleig, *J. Electrochem. Soc.*, 2017, **164**, F790–F803.

27 S. Smetaczek, A. Limbeck, V. Zeller, J. Ring, S. Ganschow, D. Rettenwander and J. Fleig, *Mater. Adv.*, 2022, **3**, 8760–8770.
28 X. Vendrell and A. R. West, *J. Electrochem. Soc.*, 2018, **165**, F966–F975.
29 L. Le Van-Jodin, F. Ducroquet, F. Sabary and I. Chevalier, *Solid State Ionics*, 2013, **253**, 151–156.
30 H. Buschmann, J. Dölle, S. Berendts, A. Kuhn, P. Bottke, M. Wilkening, P. Heitjans, A. Senyshyn, H. Ehrenberg, A. Lotnyk, V. Duppel, L. Kienle and J. Janek, *Phys. Chem. Chem. Phys.*, 2011, **13**, 21658–21659.
31 J. Fleig, *Solid State Ionics*, 2002, **150**, 181–193.
32 M. Gerstl, E. Navickas, G. Friedbacher, F. Kubel, M. Ahrens and J. Fleig, *Solid State Ionics*, 2011, **185**, 32–41.
33 X. Guo and R. Waser, *Prog. Mater. Sci.*, 2006, **51**, 151–210.
34 R. Amin and Y. M. Chiang, *J. Electrochem. Soc.*, 2016, **163**, X7.
35 J. Fleig, A. Schmid, G. M. Rupp, C. Slouka, E. Navickas, L. Andrejs, H. Hutter, L. Volgger and A. Nenning, *Acta Chim. Slov.*, 2016, **63**, 509–518.
36 C. B. Zhu, C. Wu, C. C. Chen, P. Kopold, P. A. van Aken, J. Maier and Y. Yu, *Chem. Mater.*, 2017, **29**, 5207–5215.
37 M. Morgenbesser, S. Taibl, M. Kubicek, A. Schmid, A. Viernstein, N. Bodenmüller, C. Herzig, F. Baiutti, J. D. Sirvent, M. O. Liedke, M. Butterling, A. Wagner, W. Artner, A. Limbeck, A. Tarancon and J. Fleig, *Nanoscale Adv.*, 2021, **3**, 6114–6127.
38 M. Siebenhofer, F. Baiutti, J. D. Sirvent, T. M. Huber, A. Viernstein, S. Smetaczek, C. Herzig, M. O. Liedke, M. Butterling, A. Wagner, E. Hirschmann, A. Limbeck, A. Tarancon, J. Fleig and M. Kubicek, *J. Eur. Ceram. Soc.*, 2022, **42**, 1510–1521.
39 G. M. Rupp, M. Glowacki and J. Fleig, *J. Electrochem. Soc.*, 2016, **163**, F1189–F1197.
40 M. Siebenhofer, U. Haselmann, A. Nenning, G. Friedbacher, A. E. Bumberger, S. Wurster, W. Artner, H. Hutter, Z. L. Zhang, J. Fleig and M. Kubicek, *J. Electrochem. Soc.*, 2023, **170**, 014501.
41 M. Siebenhofer, T. M. Huber, G. Friedbacher, W. Artner, J. Fleig and M. Kubicek, *J. Mater. Chem. A*, 2020, **8**, 7968–7979.
42 B. A. Boukamp and H. J. M. Bouwmeester, *Solid State Ionics*, 2003, **157**, 29–33.
43 A. Nenning, L. Volgger, E. Miller, L. V. Mogni, S. Barnett and J. Fleig, *J. Electrochem. Soc.*, 2017, **164**, F364–F371.
44 J. Ring, A. Nenning and J. Fleig, *J. Electrochem. Soc.*, 2023, **170**, 050530.
45 T. Shimonosono, Y. Hirata, Y. Ehira, S. Sameshima, T. Horita and H. Yokokawa, *Solid State Ionics*, 2004, **174**, 27–33.
46 T. Broux, B. Fleutot, R. David, A. Brull, P. Veber, F. Fauth, M. Courty, L. Croguennec and C. Masquelier, *Chem. Mater.*, 2018, **30**, 358–365.
47 R. Amin, P. Balaya and J. Maier, *Electrochem. Solid-State Lett.*, 2007, **10**, A13–A16.
48 J. S. Lee and H. I. Yoo, *Solid State Ionics*, 1994, **68**, 139–149.
49 C. Riedl, M. Siebenhofer, A. Nenning, A. Schmid, M. Weiss, C. Rameshan, A. Limbeck, M. Kubicek, A. K. Opitz and J. Fleig, *J. Mater. Chem. A*, 2022, **10**, 14838–14848.
50 J. Fleig, H. R. Kim, J. Jamnik and J. Maier, *Fuel Cells*, 2008, **8**, 330–337.
51 M. Krammer, A. Schmid, A. Nenning, A. E. Bumberger, M. Siebenhofer, C. Herzig, A. Limbeck, C. Rameshan, M. Kubicek and J. Fleig, *ACS Appl. Mater. Interfaces*, 2023, 8076–8092.
52 M. Krammer, A. Schmid, M. Siebenhofer, A. E. Bumberger, C. Herzig, A. Limbeck, M. Kubicek and J. Fleig, *ACS Appl. Energy Mater.*, 2022, 8324–8335.
53 F. S. Baumann, J. Fleig, H. U. Habermeier and J. Maier, *Solid State Ionics*, 2006, **177**, 1071–1081.
54 M. Krammer, A. Schmid, M. Kubicek and J. Fleig, *J. Power Sources*, 2023, **577**, 233167.
55 R. Amin, J. Maier, P. Balaya, D. P. Chen and C. T. Lin, *Solid State Ionics*, 2008, **179**, 1683–1687.
56 J. Illig, M. Ender, T. Chrobak, J. P. Schmidt, D. Klotz and E. Ivers-Tiffee, *J. Electrochem. Soc.*, 2012, **159**, A952–A960.
57 J. C. Jiang, W. Shi, J. M. Zheng, P. J. Zuo, J. Xiao, X. L. Chen, W. Xu and J. G. Zhang, *J. Electrochem. Soc.*, 2014, **161**, A336–A341.
58 Y. D. Liu and J. Xie, *J. Electrochem. Soc.*, 2015, **162**, A2208–A2217.
59 K. Tang, X. Q. Yu, J. P. Sun, H. Li and X. J. Huang, *Electrochim. Acta*, 2011, **56**, 4869–4875.
60 L. Li, Y. L. Xu, R. Chang, C. Wang, S. N. He and X. D. Ding, *Energy Storage Mater.*, 2021, **37**, 325–335.
61 J. K. Eckhardt, P. J. Klar, J. D. Janek and C. Heiliger, *ACS Appl. Mater. Interfaces*, 2022, **14**, 35545–35554.
62 J. Fleig and J. Maier, *Electrochim. Acta*, 1996, **41**, 1003–1009.
63 J. Fleig and J. Maier, *Solid State Ionics*, 1996, **85**, 17–24.
64 J. Fleig and J. Maier, *J. Electroceram.*, 1997, **1**, 73–89.
65 X. B. Cheng, R. Zhang, C. Z. Zhao, F. Wei, J. G. Zhang and Q. Zhang, *Adv. Sci.*, 2016, **3**, 1500213.
66 Y. L. Chu, Y. B. Shen, F. Guo, X. Zhao, Q. Y. Dong, Q. Y. Zhang, W. Li, H. Chen, Z. J. Luo and L. W. Chen, *Electrochem. Energy Rev.*, 2020, **3**, 187–219.
67 M. Steinhauer, S. Risse, N. Wagner and K. A. Friedrich, *Electrochim. Acta*, 2017, **228**, 652–658.
68 O. E. Barcia, E. D'Elia, I. Frateur, O. R. Mattos, N. Pébère and B. Tribollet, *Electrochim. Acta*, 2002, **47**, 2109–2116.
69 S. B. Adler, J. A. Lane and B. C. H. Steele, *J. Electrochem. Soc.*, 1996, **143**, 3554–3564.
70 S. Dierickx, T. Mundloch, A. Weber and E. Ivers-Tiffée, *J. Power Sources*, 2019, **435**, 69–82.
71 A. Flura, C. Nicollet, S. Fourcade, V. Vibhu, A. Rougier, J. M. Bassat and J. C. Grenier, *Electrochim. Acta*, 2015, **174**, 1030–1040.
72 Z. Siroma, N. Fujiwara, S. Yamazaki, M. Asahi, T. Nagai and T. Ioroi, *J. Electroanal. Chem.*, 2020, **878**, 114622.
73 D. Poetzsch, R. Merkle and J. Maier, *J. Power Sources*, 2013, **242**, 784–789.